



# An efficient screening of dissolution modulators of Mg alloys: Combining high-throughput multi-well exposure with topographical quantification of volume loss and pitting corrosion

Ci Song <sup>a,\*</sup>, Bahram Vaghefinazari <sup>a</sup>, Tim Wüerger <sup>a</sup>, Anna Lisitsyna <sup>b</sup>, Di Mei <sup>c</sup>, Maria Nienaber <sup>d</sup>, Jan Bohlen <sup>d</sup>, Mikhail L. Zheludkevich <sup>a,e,f</sup>, Shadi Albarqouni <sup>b,g</sup>, Christian Feiler <sup>a,f</sup>, Sviatlana V. Lamaka <sup>a,\*</sup>

<sup>a</sup> Institute of Surface Science, Helmholtz-Zentrum Hereon, Geesthacht 21502, Germany

<sup>b</sup> Helmholtz AI, Helmholtz Center Munich, Neuherberg 85764, Germany

<sup>c</sup> School of Materials Science and Engineering & Henan Key Laboratory of Advanced Magnesium Alloy, Zhengzhou University, Zhengzhou 450001, PR China

<sup>d</sup> Institute of Material and Process Design, Helmholtz-Zentrum Hereon, Geesthacht 21502, Germany

<sup>e</sup> Institute for Materials Science, Faculty of Engineering, Kiel University, Kiel 24103, Germany

<sup>f</sup> Kiel Nano, Surface and Interface Science KiNSIS, Kiel University, Kiel 24103, Germany

<sup>g</sup> University Hospital Bonn, University of Bonn, Bonn 53127, Germany

## ARTICLE INFO

**Keywords:**  
Magnesium  
Corrosion inhibitor  
Pitting factor  
High-throughput  
Screening  
Profilometry

## ABSTRACT

Experimental exploration of the vast number of potentially effective organic inhibitors presents a major bottleneck in finding suitable alternatives for chromate-based corrosion inhibitors as the quantities of these organic compounds are essentially infinite. To tackle this challenge, a multi-well experimental method for corrosion inhibitor screening has been proposed in this work. The inhibition effect and pitting factor of 229 potential inhibitors were determined by profilometric analysis using the high-throughput experiment. The accuracy is validated by traditional gravimetric weight loss analysis. The obtained results indicate that the developed approach is of great significance in accelerating the discovery and application of dissolution modulators.

## 1. Introduction

In recent decades, magnesium (Mg) and its alloys have attracted high attention in multiple applications due to their high strength-to-weight ratio, bio-absorbability, and energy-storage capabilities. They are promising to be employed in aerospace, automotive industries, medical implants, and energy storage solutions [1–5]. However, resolving the vulnerability of Mg alloys to corrosion is a vital challenge to the development and the widespread applications of Mg alloys especially for structural purposes. Alloying, surface modification, and application of dissolution modulators are three main approaches to control Mg degradation. A comprehensive list of alloying elements was summarized in [1,6] to illustrate their influences on both anodic and cathodic kinetics in Mg alloys corrosion. However, it is also necessary to consider the influence of alloying on other aspects such as mechanical properties because alloying cannot always increase the corrosion resistance and

other aspects such as mechanical properties at the same time [7,8]. Another potent and widely used method to protect Mg and its alloys from corrosion is surface modification [9–12].

Numerous chemical compounds, also called dissolution modulators, have been explored as additives to corrosive media or coatings for controlling the Mg degradation for engineering, medical implant or energy storage applications.[13–18]. Dissolution modulator is an umbrella term including corrosion inhibitors and dissolution promoters. Chemical substances that, when added in small concentrations to operational environment, prevent or minimize various forms of corrosion are considered corrosion inhibitors, while those supporting continuous degradation (for Mg-air battery applications) are considered dissolution promoters or accelerators. To further enhance the corrosion resistance, corrosion inhibitors can be incorporated into the coatings in order to confer an additional active corrosion protection effect [19–22]. Through the utilization of corrosion inhibitors, the corrosion resistance

\* Corresponding authors.

E-mail addresses: [Ci.Song@hereon.de](mailto:Ci.Song@hereon.de) (C. Song), [Sviatlana.Lamaka@hereon.de](mailto:Sviatlana.Lamaka@hereon.de) (S.V. Lamaka).

could be retained for a longer period after the coating integrity is compromised. However, due to their carcinogenicity, chromate-based inhibitors, the most known inhibitors, have been targeted for removal from the metal finishing and coatings industries in many jurisdictions including Europe and the US [16,17,23,24], the discovery of eco-friendly and effective corrosion inhibitors remains imperative [23].

Inhibition efficiency (IE) is employed in most studies to quantify the effect of dissolution modulators on metal corrosion. Based on the weight loss (WL) results, it can be defined by the following equation:

$$IE = \frac{WL_{blank} - WL_{mod}}{WL_{blank}} \times 100\% \quad (1)$$

where  $WL_{blank}$  and  $WL_{mod}$  are the weight loss of the sample after exposure to a blank corrosive solution (e.g. aqueous 3.5 wt% NaCl in this work) and in dissolution modulator-containing corrosive solution, respectively. Positive IE values indicate that corrosion is retarded while negative values mean that corrosion is accelerated [13]. Kokalj et al. recently highlighted the limitation of IE metrics due to their high nonlinearity [25], which is not convenient to differentiate between strong inhibitors. Therefore, another metric, inhibition power (IP), possessing higher linearity was introduced by Kokalj et al., which is defined as follows [25]:

$$IP = 10 \log_{10} \frac{R_p^{mod}}{R_p^{blank}} \quad (2)$$

where  $R_p^{mod}$  is the polarization resistance of the sample in dissolution modulator-containing corrosive solution and  $R_p^{blank}$  is the polarization resistance of the sample in blank NaCl solution. The equation above can also be adapted for using the WL results:

$$IP = 10 \log_{10} \frac{WL_{blank}}{WL_{mod}} \quad (3)$$

The IP allows for better differentiation between highly efficient corrosion inhibitors,  $IE > 90\%$ . Another metric, symmetrized inhibition efficiency ( $IE_{sym}$ ), was also recently proposed by Kokalj et al. [26] and scales negative values of IE to a range between 0 and  $-100\%$ . This metric provides a more intuitive and balanced presentation of negative IE values, which are common for highly reactive magnesium alloys, often skewing large datasets of corrosion inhibition values. The  $IE_{sym}$  spans from  $-100\text{--}100\%$ , offering a balanced view of both inhibitors and dissolution promoters. The equation for  $IE_{sym}$  is as follows [26]:

$$IE_{sym} = \begin{cases} IE; \text{if } IE \geq 0 \\ -\frac{WL_{mod} - WL_{blank}}{WL_{mod}} \times 100\%; \text{otherwise} \end{cases} \quad (4)$$

Magnesium is one of the least noble engineering metals. This makes it susceptible to micro-galvanically driven or micro-structure controlled localized corrosion, sometimes manifested as pitting like corrosion [27, 28]. It has been reported that the mechanical properties of Mg alloys can be significantly reduced after corrosion due to severe localized corrosion, although their corrosion rate is relatively low [29,30]. Therefore, the evaluation of corrosion inhibitors for Mg alloy should not only be limited to their corrosion inhibition effects, but also consider the influence of corrosion inhibitors on the localized corrosion of Mg alloy.

Organic molecules represent an immense space to screen suitable dissolution modulators for Mg alloys in various applications. One of the most comprehensive databases of dissolution modulators for Mg alloys has been published by Lamaka et al., in which IEs of 151 chemical dissolution modulators for six Mg alloys (AZ31, AZ91, AM50, WE43, ZE41, and E21) and three grades of pure Mg have been tested [13]. Several highly efficient inhibitors such as several pyridinedicarboxylate derivatives, fumarate, quinaldate, and several methyl-, nitro-, and amino-salicylates were discovered, and their inhibition mechanisms have been scrutinized [13], highlighting the importance of

comprehensive screening. However, the high experimental effort and costs of testing a huge number of dissolution modulators by traditional immersion methods are prohibitive for one-by-one testing of dissolution modulators. There are approximately 120 million molecules [31] that have been already reported and catalogued in the CAS (chemical abstract service) database. Furthermore, the number of potentially synthesizable organic molecules could be projected to reach an astonishing  $10^{80}$  [32]. Consequently, screening for suitable dissolution modulators from these molecules is a challenging task, and seeking the whole space is experimentally practically impossible. Several studies have demonstrated the possibility to employ machine learning (ML) methods, involving descriptors derived from chemoinformatic software packages in combination with density functional theory calculations, to predict the IE of organic dissolution modulators for metallic surfaces [33–37], thus facilitating the discovery of unknown organic dissolution modulators by short-listing promising candidates for testing. However, these methods also require large, reliable, chemically diverse and balanced training data sets to make accurate predictions for a broad range of dissolution modulators [33]. Consequently, rapid generation of required large libraries is still an essential issue to accelerate the discovery and optimization of suitable dissolution modulators. A new large machine-readable database containing over 1300 individual organic molecules with corrosion inhibition function tested for Al, Cu, Mg and steels has been released recently [16]. Along with that, state of the art in inhibition mechanisms is summarized and linked with overview of data-driven quantitative structure–property relationships models towards faster screening and computational discovery of efficient corrosion inhibitors.

A number of high-throughput methods for testing dissolution modulators IE have been proposed in recent years. Chambers [38] and Muster [39] demonstrated the use of multi-electrode array as the means to carry out high-throughput electrochemical corrosion testing for obtaining IE values of different dissolution modulators on different materials. Then, Kallip [40] employed a multi-material electrode cell combined with Scanning Vibrating Electrode Technique (SVET) to test the inhibition effect of several organic and inorganic compounds a multi-material electrode, composed of Mg, Zn, Al, Cu, and stainless steel. This allowed simultaneous assessment of localized cathodic and anodic currents by SVET on these metals in one testing solution [40]. With respect to immersion experiments, White [41] and Winkler [34] developed a multi-well device to simultaneously expose a metal surface to several electrolytes confined to the volume of the wells. The experimental IE values of dissolution modulators on aluminium alloys were evaluated by image analysis, showing a good agreement with same duration 24-hour immersion tests, followed by weight loss validation. Zabula et al. [42] employed cold rolled steel samples with small size ( $2.54 \times 1.08 \times 0.10 \text{ cm}^3$ ) and 96 testing tubes filled with testing solutions (1 sample and 15 mL solution for each testing tube) followed by thiocyanate-based quantification of  $\text{Fe}^{3+}$  concentration as a measure of corrosion rate, achieving high-throughput screening of dissolution modulators. White et al. [43] employed a high-throughput optical method reported in their earlier work [41] and a multi-channel electrochemical potentiostat to rapidly identify effective corrosion inhibitors [43]. Qiu et.al. [44] put forward another image analysis method to rate the Mg corrosion. Mg specimens were embedded in an epoxy resin and fixed at the bottom of each cell of a  $5 \times 5$  multi-well plate filled with the testing solution. To calculate the IE values, optical photos of corroded surfaces were captured and processed into binary images, in which the dark areas formed on the Mg surface were regarded as corroded zones and the remaining areas as inhibited zone [44].

It is also worth noting that the above-mentioned high-throughput studies employ a low ratio between solution volume and sample surface area ( $0.7 \sim 6 \text{ mL}\cdot\text{cm}^{-2}$ ), which can yield significantly different corrosion results compared with those performed in full immersion [45], typical for conventional laboratory corrosion experiments (e.g., EIS, PDP, LPR or hydrogen evolution measurement for Mg alloys). However,

it is still valuable to evaluate the inhibition effect of dissolution modulators in such corrosion conditions because a small volume of corrosive solution on bulk Mg alloys is more representative of service environments than full immersion, e.g., wet and dry cycles during atmospheric corrosion. In most real-world applications, metallic parts are not fully immersed, experiencing only periodic contact with corrosive electrolytes or thin condensation electrolyte films [46]. In traditional laboratory immersion tests, including the common H<sub>2</sub> evolution test for Mg alloys, relatively high ratio between solution volume and sample surface area are commonly used. Therefore, any change in the electrolyte composition due to the corrosion process (e.g., consumption of dissolution modulators and alkalization) occurs at a slower rate. Furthermore, a high ratio of solution volume to sample surface area may provide a higher amount for many components in the solution (especially the tested dissolution modulator), but a lower concentration of oxygen to support the ORR, which is less representative of a practical application condition. Therefore, targeting minimal solution volume to sample surface area ratios in corrosion studies is crucial to closely replicate the service environment of Mg alloys.

Topographic surface analysis with a profilometer, employing light-section method, is able to quantify the surface roughness induced by the corrosion process. The material volume loss due to corrosion can be quantified and converted to weight loss results as well as IE values. At the same time, topographic surface analysis also helps to qualitatively analyse the localized corrosion of Mg alloys under the action of modulators [30], and is beneficial for more comprehensively evaluating their effects. In the current study, we combined a high-throughput multi-well immersion method with topographic surface analysis to produce corrosion marks in the presence of multiple dissolution modulators and calculate their inhibition effect and pitting factor values. Over 200 individual organic chemical dissolution modulators were tested for the AZ31 alloy. These dissolution modulators include those previously reported in [13,33] as well as newly proposed according to the carboxyl-, amino-, sulfo-, phosphonate-, thiol-, or other functional groups they contain that may interact with Mg/MgO/Mg(OH)<sub>2</sub>/Mg<sup>2+</sup>. The highlight of this work lies in implementing a reliable way to rapidly quantify the inhibition effect along with quantifying respective corrosion localization in the presence of dissolution modulators for Mg alloys, greatly facilitating the establishment of a large database that can be linked to ML methods for concurrent *in silico* screening by providing the experimental foundation for the development of data-driven models. Metrics related to localized corrosion, which present the influence of various dissolution modulators on the corrosion profile of AZ31 alloy, can be readily extracted from the topographical data.

## 2. Experimental

### 2.1. Materials and compounds

All compounds were purchased from commercial suppliers (Sigma-Aldrich, Thomas Scientific, Merck, Carl Roth and Alfa Aesar) and used without further purification. The amount required to prepare a 50 mM solution of each compound was dissolved in 3.5 wt% NaCl solution. The pH of the solution was adjusted to 7.0 ± 0.5 by 1 M NaOH or in rare cases by 1 M HCl solution. With respect to some dissolution modulators with solubility lower than 50 mM, their saturated solutions were obtained by filtering undissolved dissolution modulators from the turbid solution. These cases are labelled “saturated” in Table S2.

An AZ31 extruded Mg alloy was used as the substrate. The extruded Mg alloy samples were produced as described in the previous work [47]. The elemental composition is listed in Table S1. Extruded AZ31 strips with a cross-section of 15 mm × 2 mm were cut into pieces with a length of 80 mm. These samples were initially ground with emery papers (Hermes) from 800 grit, 2500 grit, and finally to 4000 grits. Then, the samples were immersed in an acid pickling solution composed of sodium nitrate (50 g/L) and acetic acid (200 g/L) to remove impurities and

corrosion products from Mg surface [48,49]. As shown in Fig. S1, during acid pickling treatment, one group, consisting of six samples (six strips of magnesium alloy) were hung by plastic-wrapped wires on a glass rod, with the sample surface positioned at a 45-degree angle from the surface of the acid solution during the treatment. Distance between samples remained fixed (approximately 1 cm) to make sure samples could be in contact with a sufficient amount of acid solution. Freshly prepared 500 mL solution was used every time to ensure the consistency of the acid pickling treatment. After 1 minute of immersion with stirring, the samples were immersed in deionized water (500 mL), stirred for two times (every time for 30 seconds) and then cleaned with ethanol. Eventually, the samples were dried in a pressured air flow at room temperature.

### 2.2. High-throughput exposure experiment

The multi-well device is presented in Fig. 1. It consists of two polymethyl-methacrylate (PMMA) plates and one silicone rubber plate. The silicone rubber plate was placed on the Mg strips, aligned and clamped together with six screws between the two PMMA plates. Both the silicone rubber plate and the PMMA plate on top of it have coaxial holes with a diameter of 10 mm in an array of 4 × 6. The holes were filled with 1 mL of the testing solution. During each round of the experiment, six Mg strips were tested as one group, and four corrosion marks were produced on each strip for one dissolution modulator. The process for placing samples and setting up the high-throughput device takes about 30 minutes. In each group, one sample was always tested by adding blank 3.5 wt% NaCl solution to four wells belonging to one strip. Five other strips of the same group were used to test five individual dissolution modulators (50 mM) dissolved in 3.5 wt% NaCl solution. In total one testing group produced 4 × 6 corrosion marks. The reference sample tested in blank NaCl solution was included in each group to accumulate sufficient number of parallel tests for a reliable reference corrosion performance and to account for any small experimental variation for each 6-sample group, such as differences in grinding quality, acid etching, chromic acid quality, temperature variation, etc. During exposure measurements, the high-throughput experimental device was placed together with the samples in a constant temperature and humidity chamber to sustain a similar temperature and no evaporation of solutions for all exposure measurements. The room temperature during the immersion was 22 ± 2 °C with a humidity of 75 ± 5 %. After 24 hours of exposure, samples were taken out from the multi-well device, rinsed with deionized water and ethanol, and then dried immediately with pressurized air. The removal of the corrosion products was carried out via immersion of the samples in a chromic acid solution (aqueous solution of CrO<sub>3</sub>, 200 g/L) for 5 minutes. The effectiveness of chromic acid in removing the corrosion products without etching the Mg substrate is related to the amount of corrosion products it has removed. Accumulated chlorides in the acidic environment of chromic acid prevent surface passivation, inducing additional corrosion during removal of corrosion products. To prevent this, only six samples in one group together were immersed in 200 mL chromic acid solution every time to ensure the same effect of chromic acid on all samples. After cleaning four groups of samples (4 × 6 individual samples in total), chromic acid was discarded, and a freshly prepared chromic acid solution was used for the next batch.

### 2.3. Topography and profile detection

The overall process of the experiments in this paper is schematically summarized in Fig. 2. The samples in the multi-well setup were exposed to 3.5 wt% NaCl with or without dissolution modulators. A profilometer (VR-5000, Keyence) was used to obtain topography maps of the sample surfaces (before and after removing the corrosion products with the chromic acid solution). The profilometric volume loss in this study was calculated solely from the specimen after removing corrosion products

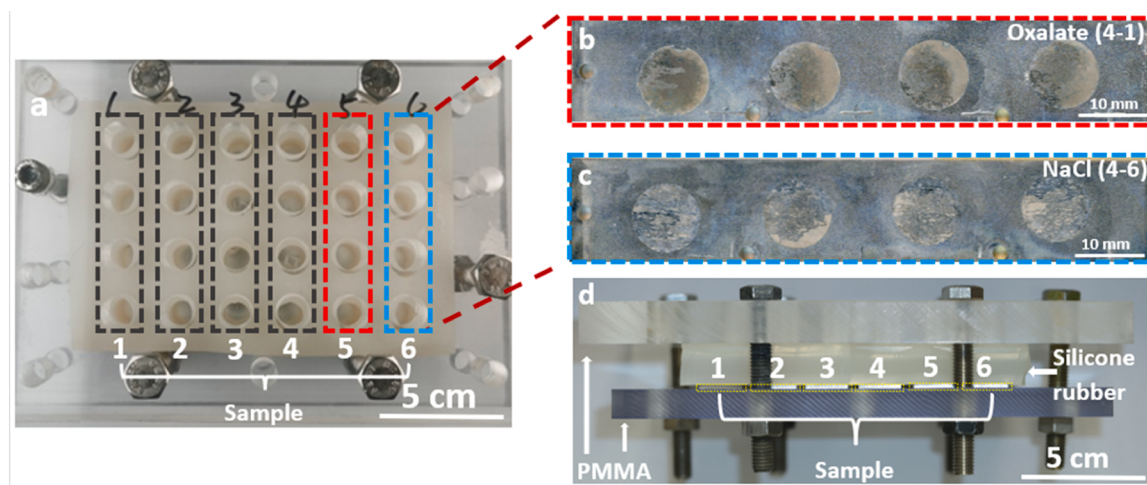


**Fig. 1.** **a** Top view of the multi-well device; **b** and **c** are examples of the samples exposed to the blank NaCl solution with and without sodium oxalate before chromic acid cleaning, respectively; **d** side view of the multi-well device. Rough surface appearance around the corrosion marks is due to the acid pickling pre-treatment explained in 2.1.

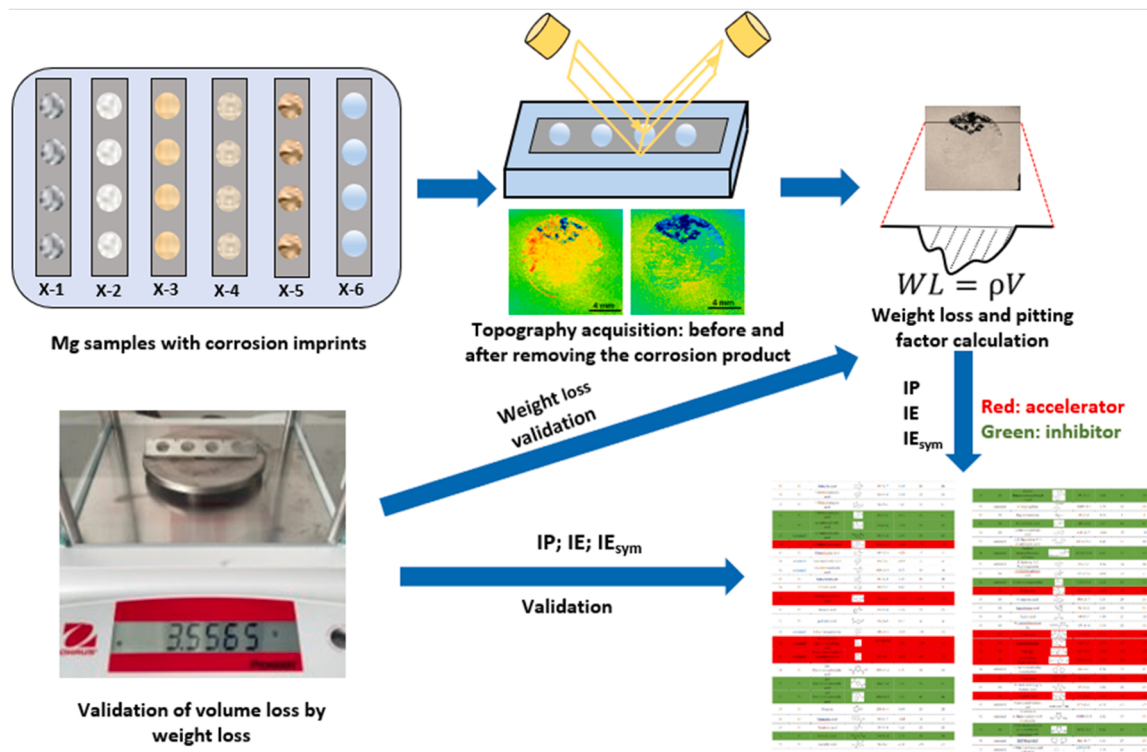


**Fig. 2.** Schematic of experimental workflow to evaluate inhibition effect of tested dissolution modulators.

with chromic acid. Using the uncorroded surface area as the zero-height reference plane, the volume loss of the corroded area after removing the corrosion products was calculated by light-section method. The volume loss was converted to the weight loss by using the density of AZ31 alloy, which is  $1.78 \text{ g/cm}^3$ . The obtained volume loss by the profilometer and the corresponding calculated weight loss are denoted as  $\mathbf{P(V)}$  and  $\mathbf{P}$ , respectively. Optical magnification of  $40 \times$  (reported resolution in X and Y direction is  $7.4 \mu\text{m}$ , in Z direction is  $0.1 \text{ nm}$ ) on the profilometer was used to collect the results from all marks. Topographic quantification of each individual corrosion circle area took 30 seconds. The scanned area during each profilometry scan is  $1.2 \times 1.2 \text{ cm}^2$ , which is larger than the corroded circle area ( $0.785 \text{ cm}^2$ ). Based on the calculated weight loss result of four marks for each sample, the values of inhibition

efficiency (IE), symmetrized inhibition efficiency ( $\mathbf{IE}_{\text{sym}}$ ), and inhibition power (IP), were calculated. The pitting factor (PF) values were also calculated based on the profilometric results of corrosion depth distribution. The equations for calculating average values of these inhibition effects evaluating metrics and their corresponding standard deviations (StDev) are defined as follows:

$$\mathbf{IE}_x = \frac{\overline{WL}_{\text{blank}} - WL_{\text{mod}-x}}{\overline{WL}_{\text{blank}}} \times 100\% \quad (5)$$

$$\mathbf{IE}_{\text{sym},x} = \begin{cases} \mathbf{IE}_x; & \text{if } \mathbf{IE}_x \geq 0 \\ -\frac{WL_{\text{mod}-x} - \overline{WL}_{\text{blank}}}{WL_{\text{mod}-x}} \times 100\%; & \text{otherwise} \end{cases} \quad (6)$$

$$IP_x = 10 \log_{10} \frac{\overline{WL}_{blank}}{WL_{mod-x}} \quad (7)$$

$$PF_x = \frac{\text{Maximum depth}_x}{\text{Average depth}_x} \quad (8)$$

$$StDev_y = \sqrt{\frac{\sum_{x=1}^4 (y_x - \bar{y})^2}{(n-1)}} \quad (9)$$

where  $x$  denotes the serial number of mark (from 1 to 3 or 4 depending on the number of marks tested by each dissolution modulators) or average; therefore, for a specific sample,  $IE_x$ ,  $IE_{sym,x}$ ,  $IP_x$ , and  $PF_x$  represent the individual or the average value of four respective marks for these three metrics;  $WL_{mod-x}$  denotes the individual or the average value of four respective marks for the weight loss in case of the dissolution modulator tested sample;  $\overline{WL}_{blank}$  indicates the average weight loss results of four marks for the reference sample in the corresponding group; PF is calculated by ASTM G46-94 (Eq. 9) [50]; taking uncorroded surface as zero-height reference plane, *Maximum depth* represents the maximum depth of the corrosion pit detected by profilometry and *Average depth* indicates the average depth of the corroded area provided by profilometry;  $y$  denotes the individual value of  $IE$ ,  $IE_{sym}$ , IP, pitting factor (PF) or corroded area ratio;  $n$  indicates the number of marks tested by each dissolution modulators (most of them

are 4 and few are 3).

The weight loss determined based on the volume loss was validated by regular weight loss measurement using an analytical balance (Sartorius AX224, resolution is 0.1 mg). The validation process was conducted across five groups of samples (tested first chronologically) to ensure the accuracy and reliability of profilometric results. As mentioned above, each group contains 5 or 6 stripes, for a total of 29 strips. 24 strips were tested with NaCl solutions with 24 individual dissolution modulators and 5 strips were tested with dissolution modulator-free NaCl solution.

Before and after chromic acid cleaning, the visual appearance of the corrosion marks was documented by collecting optical images. For this purpose, a table-top scanner, Epson Perfection V850 Pro was used. The resolution of the scanned picture is 3200 dpi. The contrast for each sample was adjusted before each scan to achieve optimal light balance for each sample. The optical images and profilometric maps of corroded surfaces acquired before removing the corrosion products were collected for the follow up research that builds an image recognition machine learning model predicting the corrosion impact solely from evaluation of visual appearance of corroded surface.

The morphology of selected samples after chromic acid cleaning was characterized by SEM (VEGA TESCAN). For cross-section preparation, the samples were embedded in transparent epoxy (Buehler; epoxy harder, 20-3432-032; epoxy resin 20-3430-128) and ground upon solidification to the desired position, followed by polishing. Polishing was applied on a polishing disc (80 r/min) with diamond slurry (1 μm

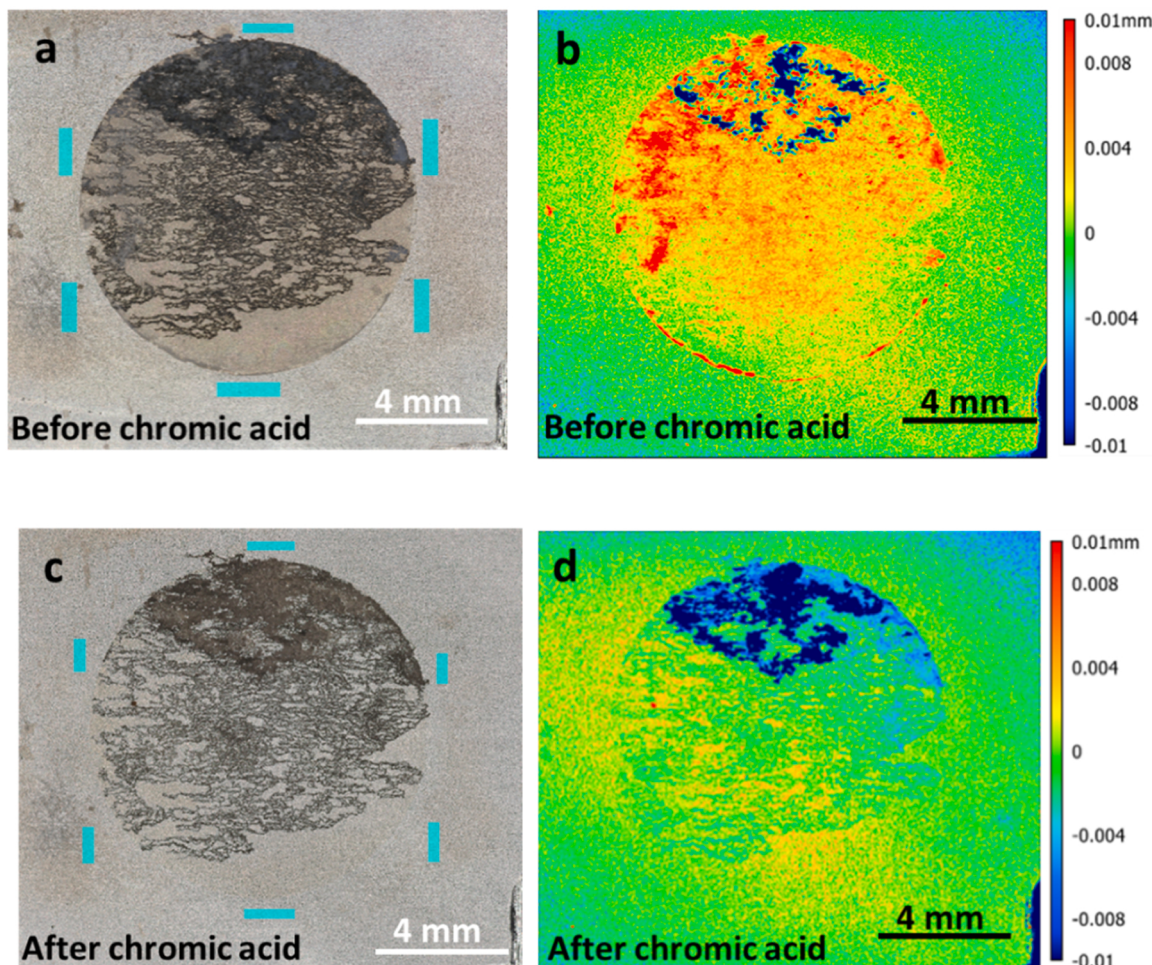


**Fig. 3.** **a** and **b** show the representative optical image of a sample exposed to blank 3.5 wt% NaCl solution (coded NaCl (1–6)) and the corresponding topographic map before the removal of the corrosion product; **c** and **d** show the optical image and topographic map of the respective sample after removing the corrosion product. Rectangle marks in the optical images indicate the reference plane.

diameter, Metallographie GmbH) and oxide polishing suspension (OPS, Industrial service Siegmund Bigott) solution. The samples were sputter coated with gold (Cressington Sputter Coater) before the SEM characterization to achieve better electrical conductivity and avoid charge accumulation. The accelerating voltage used in SEM is 15 kV.

### 3. Results

#### 3.1. Volume loss quantification by topographic analysis

**Fig. 3 a** and **c** show the optical images of a single corrosion mark tested in blank 3.5 wt% NaCl before and after removing the corrosion products using chromic acid solution. The corresponding topography maps are shown in **Fig. 3 b** and **d**. To define the reference plane, six areas were selected around the corrosion mark in the uncorroded zone in **Fig. 3 a** and **c**. As can be seen in the topography maps in **Fig. 3**, the localized corrosion has been captured on the corrosion mark, indicating that the weight loss can be acquired by quantification of the three-dimensional surface profile. From the comparison of these two groups of images, it can be seen that the corrosion product is effectively removed by chromic acid.

#### 3.2. Optical images

The exemplary optical images of corrosion marks are shown in **Fig. 1 b** and **c**. Additional sets of optical images for the first five groups before and after removing the corrosion product are shown in **Figure S2**. The samples exposed to different dissolution modulators show different appearances, and colour shades after the corrosion products are removed by chromic acid.

#### 3.3. Inhibition efficiency, symmetrized inhibition efficiency, and inhibition power results

All dissolution modulators tested in this paper are summarized in **Supplementary Materials Table S2**, along with their corresponding CAS numbers, concentrations, IE,  $IE_{sym}$ , IP values calculated by P, (hereafter referred to IE-P,  $IE_{sym}$ -P, and IP-P), and PF. A total of 229 dissolution modulators were tested, all listed in **Table S2** with corresponding results. For easier display and reading, these results are also shown in **Fig. 4** and **Fig. 5**. The results shown in **Table S2**, **Fig. 4** and **Fig. 5** are average IE,  $IE_{sym}$ , IP, PF with corresponding StDev, calculated by the profilometric results from four marks for every sample as mentioned above (**Section 2.3; Eqs. 5, 6, 7, 8, and 9**).

**Fig. 4** shows the  $IE_{sym}$  results of all dissolution modulators tested in this study. **Fig. 4 (a)** presents those dissolution modulators with  $IE > 50\%$ , **Fig. 4 (b)** those with  $-40\% < IE < 50\%$  and the remaining dissolution modulators with  $IE < -40\%$  are shown in **Fig. 4 (c)**. Since  $IE_{sym}$  allows for a more intuitive comparison of the inhibition effects for dissolution modulators (detailed comparison and discussion will be shown in **Section 3.4.2**), the X-axis in these three figures is  $IE_{sym}$  instead of IE. According to the order of  $IE_{sym}$  values from high to low, tested dissolution modulators are arranged from top to bottom in the Y-axis direction in all three figures. Notably, 1,3,4-thiadiazole-2,5-dithiol (also known as DMTD or bismuthiol [51]) presents the best inhibition effect (IE: 87 %,  $IE_{sym}$ : 87 %, and IP: 9.02), while ethylenediamine shows the worst inhibition effect (IE: -454 %,  $IE_{sym}$ : -82 %, and IP: -7.43). Besides, SDBS (IE: 77 %,  $IE_{sym}$ : 77 %, and IP: 6.43), 2,5-thiophenedicarboxylic acid (IE: 74 %,  $IE_{sym}$ : 74 %, and IP: 5.89), thiourea (IE: 72 %,  $IE_{sym}$ : 72 %, and IP: 5.6), 5-aminosalicylic acid (IE: 63 %,  $IE_{sym}$ : 63 %, and IP: 4.35), 1,2,4-benzenetricarboxylic acid (IE: 63 %,  $IE_{sym}$ : 63 %, and IP: 4.31), 5-aminoisoquinoline (IE: 62 %,  $IE_{sym}$ : 62 %, and IP: 4.26), 5-methylsalicylic acid (IE: 61 %,  $IE_{sym}$ : 61 %, and IP: 4.13), 5-amino-1,3,4-thiadiazole-2-thiol (IE: 59 %,  $IE_{sym}$ : 59 %, and IP: 3.90), and fumaric acid (IE: 58 %,  $IE_{sym}$ : 58 %, and IP: 3.75) are the next nine dissolution modulators showing the next highest corrosion inhibition effects. All of

these dissolution modulators will be discussed in this **Section 3.3**. Except for SDBS [13,52–54], 1,3,4-thiadiazole-2,5-dithiol [13], thiourea [13], and 5-aminosalicylic acid [13], for six out of these ten dissolution modulators, it is the first time to be mentioned as corrosion inhibitors for Mg alloys. As mentioned in the introduction section, the range of  $IE_{sym}$  is between -100 % and 100 %, which is different from the range of IE. Because the inhibition effect results calculated as  $IE_{sym}$  can be evenly distributed in the figure, this graphical representation allows for a more intuitive and clear display of the values and rankings of the inhibition effect for all tested dissolution modulators.

It can be seen that the IEs values on average presented in this study are not very high (only DMTD present IE value higher than 80 %). One of the reasons should be related to the tested alloy composition. For instances, in [13], for similar concentration, sodium dodecylbenzene sulfonate (50 mM) present a 93 % of IE for CP Mg-220 ppm (commercial pure Mg containing 220 ppm of iron) while 63 % of IE for AZ31 alloy; 2,3-pyridinedicarboxylate (50 mM) exhibits a IE of 98 % for HP Mg-50 ppm (high pure Mg containing 51 ppm of iron) but 62 % of IE for AZ31 alloy, etc... It has been shown that the iron contents can influence the inhibition effects of certain dissolution modulators [13].

In terms of AZ31 alloy, some dissolution modulators such as 2-hydroxy-1,4-Naphtoquinone (40 mM), 2,5-pyridinedicarboxylate (50 mM), 3,4-pyridinedicarboxylate (50 mM and 38 mM), quinaldate (50 mM), 5-aminosalicylate (50 mM), and fumarate (50 mM) present IE values higher than 80 % in [13]. As evidenced by prior studies, benzotriazole [55,56], 8-hydroxyquinoline [54,57], and stearate [58] etc. exhibit significantly higher inhibition efficiencies compared to the values reported herein. Multiple reasons can cause discrepancies between inhibition efficiencies of the same compounds acquired at different experimental conditions. Beyond intrinsic alloy composition, these reasons include alloy microstructure, surface condition, composition and concentration of corrosive medium and inhibitor concentration, initial pH and sample surface to electrolyte volume ratio, electrolyte flow and thickness, aeration, CO<sub>2</sub> content and temperature etc... [16]. The primary objective of this study is to develop a new high-throughput screening methodology aimed at screening effective dissolution modulators for Mg alloys and we will continue testing in the follow up work.

The PF values for all tested 229 dissolution modulators are shown in **Fig. 5**. It can be seen that dissolution modulators with higher inhibition efficiencies tend to present higher PF values. The most interesting compounds with low pitting factor values and positive inhibition efficiencies are DMTD (IE: 87 %; PF: 5.4) and sodium phosphite (IE: 45 %; PF: 10.9), marked by red stars in **Fig. 5**. These compounds combine high IE with low extent of localized corrosion, the properties essential for efficient corrosion inhibitor, preserving mechanical integrity of metallic substrate [30]. In practical application, homogeneous corrosion has less impact on the service life of Mg alloys than localized corrosion in most cases. Therefore, the search should continue for corrosion inhibitors that result in slow and homogeneous degradation of Mg alloys. From this principle, DMTD and sodium phosphite are the corrosion inhibitors that closer match these requirements. For most other inhibitors, although their PF values are higher than 20.0, these might change significantly when combined with surface pretreatment (like PEO) and coatings.

As previously introduced, compared with the traditional immersion methods, using a low ratio of solution volume to the tested surface area in the current study decreases the amount of corrosive ions (especially Cl<sup>-</sup>) and the amount of inhibitor, but increases the amounts of dissolved CO<sub>2</sub> and O<sub>2</sub> from air reaching the Mg surface, which is closer to service environments of many practical applications. Therefore, IP, IE, and  $IE_{sym}$  results for certain dissolution modulators may be significantly different from those reported in previous studies. The criteria of compound selection in this study are based on the functional groups contained in the molecules. Various functional groups that can form chemical bonds with metal cations (Mg<sup>2+</sup>, Fe<sup>2+/3+</sup>, Al<sup>3+</sup>), such as carboxyl-, amino-, hydroxyl-, sulfo-, mercapto-, and phosphonate-groups, were considered.

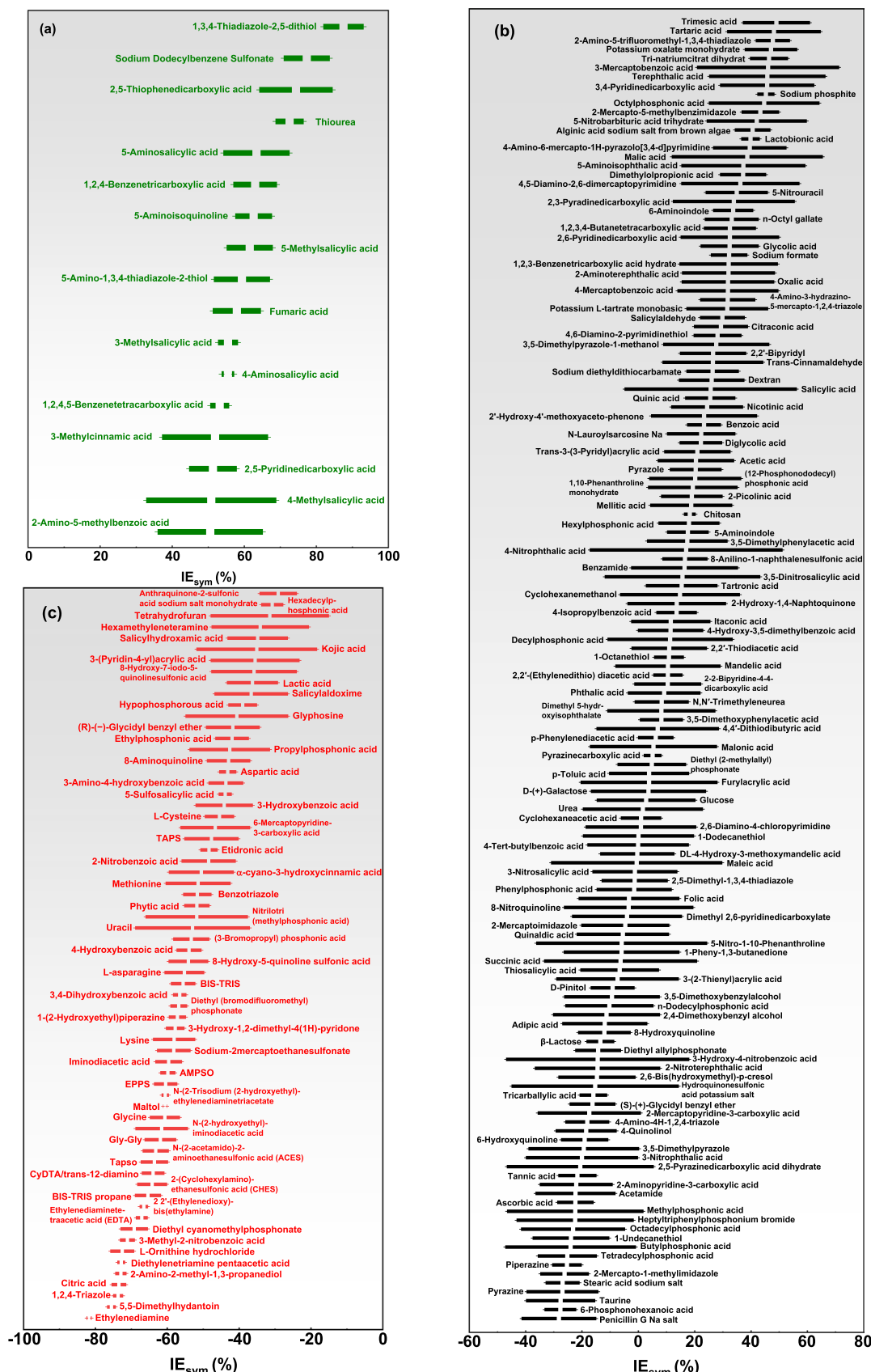


**Fig. 4.** Symmetrized inhibition efficiency (IE<sub>sym</sub>) results of 229 dissolution modulators tested in this study: dissolution modulators with inhibition efficiency (IE) > 50 % (a), -40 % < IE < 50 % (b), and IE < -40 % (c).

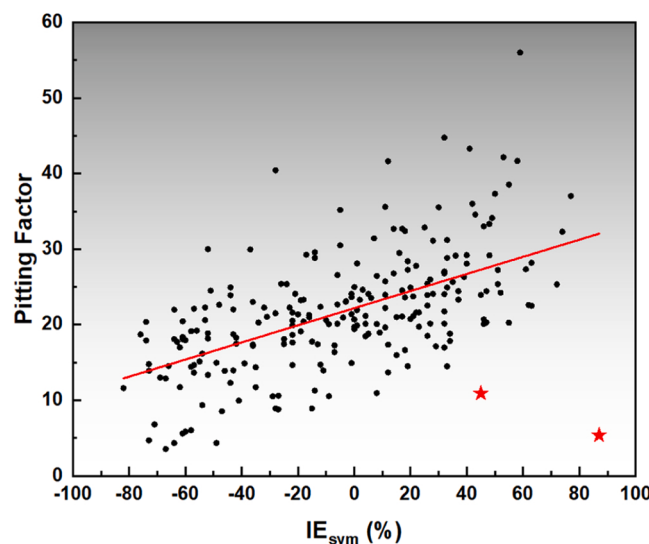


**Fig. 5.** Pitting factor of samples tested by 229 dissolution modulators tested in this study according to Eq. 8 and ASTM G46-94 [50].

Meanwhile, the molecular weight of selected compounds was mostly kept below 300 Da to facilitate the analysis and subsequent modelling.

The corrosion-accelerating effect of some dissolution modulators on Mg such as benzotriazole, observed in this work, is in line with that previously reported in [13]. However, there is a discrepancy with a previous testing campaign when comparing IE values for other dissolution modulators especially for 3-methyl-2-nitrobenzoic acid (IE: -248 % in Fig. S2 and Fig. 4 and 43 % in [13]). The material used in this study is extruded bulk AZ31 alloy, whereas [13] used chips of cast AZ31 alloy. Therefore, there is a difference between the surface area to electrolyte volume ratio in this study ( $1 \text{ mL} \cdot \text{cm}^{-2}$ ) and the previous report [13] ( $4.48\text{--}7.30 \text{ mL} \cdot \text{cm}^{-2}$ ). This leads to different profiles of pH increase and  $\text{O}_2$  and  $\text{CO}_2$  availability. Moreover, the processing history of the alloy significantly influences the microstructure and hence the inhibition effect of dissolution modulators on Mg corrosion. These controversial results further demonstrate that the inhibition effect of dissolution modulators is highly sensitive to testing/application conditions on the site of the electrolyte and metallic substrate.

The results shown in this paper are consistent with those in [13],

that EDTA (IE: -205 %,  $\text{IE}_{\text{sym}}$ : -67 %, and IP: -4.85), 3,4-dihydroxybenzoic acid (IE: -131 %,  $\text{IE}_{\text{sym}}$ : -57 %, and IP: -3.63), and phytic acid (IE: -108 %,  $\text{IE}_{\text{sym}}$ : -52 %, and IP: -3.18) are powerful accelerators. Other dissolution modulators with negative IE values, such as 1,2,4-triazole (IE: -283 %,  $\text{IE}_{\text{sym}}$ : -74 %, and IP: -5.83), 5,5-dimethylhydantoin (IE: -312 %,  $\text{IE}_{\text{sym}}$ : -76 %, and IP: -6.15), and maltol (IE: -155 %,  $\text{IE}_{\text{sym}}$ : -61 %, and IP: -4.06), are also consistent with previous results reported in [13], as summarized in Table S2 and Fig. 4.

### 3.3.1. Amino- or sulfo-containing dissolution modulators

A powerful complexing agent, ethylenediamine, exhibits the highest corrosion acceleration effect (IE: -454 %,  $\text{IE}_{\text{sym}}$ : -82 %, and IP: -7.43) on AZ31 Mg. Similarly, other dissolution modulators containing amino-group such as L-asparagine (IE: -124 %,  $\text{IE}_{\text{sym}}$ : -55 %, and IP: -3.50), uracil (IE: -113 %,  $\text{IE}_{\text{sym}}$ : -53 %, and IP: -3.29), and glycyl-glycine (IE: -164 %,  $\text{IE}_{\text{sym}}$ : -62 %, and IP: -4.21), exhibit negative IE values. As shown in Table S2 and Fig. 4, and Fig. 6, for some aliphatic carboxylates, when substituted with amino-group(s), the inhibition performance significantly decreases: succinic acid (IE: -7 %,  $\text{IE}_{\text{sym}}$ : -6 %, and IP: -0.28) in contrast to ethylenediamine (IE: -454 %,  $\text{IE}_{\text{sym}}$ : -82 %, and IP: -7.43); Tartaric acid (IE: 48 %,  $\text{IE}_{\text{sym}}$ : 48 %, and IP: 2.86) in contrast to L-asparagine (IE: -124 %,  $\text{IE}_{\text{sym}}$ : -55 %, and IP: -3.50); sodium formate (IE: 32 %,  $\text{IE}_{\text{sym}}$ : 32 %, and IP: 1.20) in contrast to urea (IE: 2 %,  $\text{IE}_{\text{sym}}$ : 2 %, and IP: 0.07); acetic acid (IE: 21 %,  $\text{IE}_{\text{sym}}$ : 21 %, and IP: 1.00) in contrast to acetamide (IE: -22 %,  $\text{IE}_{\text{sym}}$ : -22 %, and IP: -1.09); malic acid (IE: 39 %,  $\text{IE}_{\text{sym}}$ : 39 %, and IP: 2.13) in contrast to aspartic acid (IE: -76 %,  $\text{IE}_{\text{sym}}$ : -43 %, and IP: -2.46). These results indicate the amino-group presented in aliphatic dissolution modulators has a corrosion-accelerating effect for AZ31 alloy in most cases.

For aromatic dissolution modulators containing amino-group, as shown in Table S2 and Fig. 4, and Fig. 7 from 2,3-pyridinedicarboxylic acid (IE: 34 %,  $\text{IE}_{\text{sym}}$ : 34 %, IP: 1.81) to 2-aminopyridine-3-carboxylic acid (IE: -28 %,  $\text{IE}_{\text{sym}}$ : -22 %, IP: -1.08), the inhibition effect is decreased when amino-group replaces carboxylate-group. However, when terephthalic acid (IE: 46 %,  $\text{IE}_{\text{sym}}$ : 46 %, IP: 2.67) is compared to 2-aminoterephthalic acid (IE: 32 %,  $\text{IE}_{\text{sym}}$ : 32 %, IP: 1.68); salicylic acid (IE: 26 %,  $\text{IE}_{\text{sym}}$ : 26 %, IP: 1.30), 4-methylsalicylic acid (IE: 51 %,  $\text{IE}_{\text{sym}}$ : 51 %, IP: 3.07), and 5-methylsalicylic acid (IE: 61 %,  $\text{IE}_{\text{sym}}$ : 61 %, IP: 4.13) are compared to 4-aminosalicylic acid (IE: 55 %,  $\text{IE}_{\text{sym}}$ : 55 %, IP: 3.50) and 5-aminosalicylic acid (IE: 63 %,  $\text{IE}_{\text{sym}}$ : 63 %, IP: 4.35), as presented in Table S2, Fig. 8 and Fig. 9, after the hydrogen atom or methyl-group is substituted by amino-group, their inhibition effects

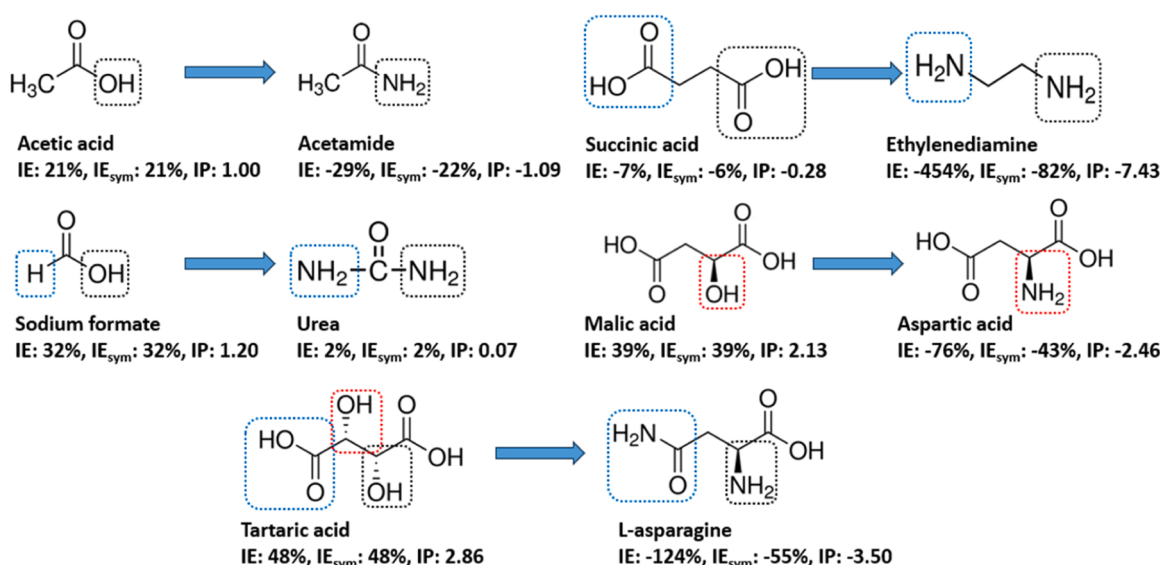


**Fig. 6.** The molecule structures and inhibition effects of aliphatic carboxylates before and after substituted with amino group(s).

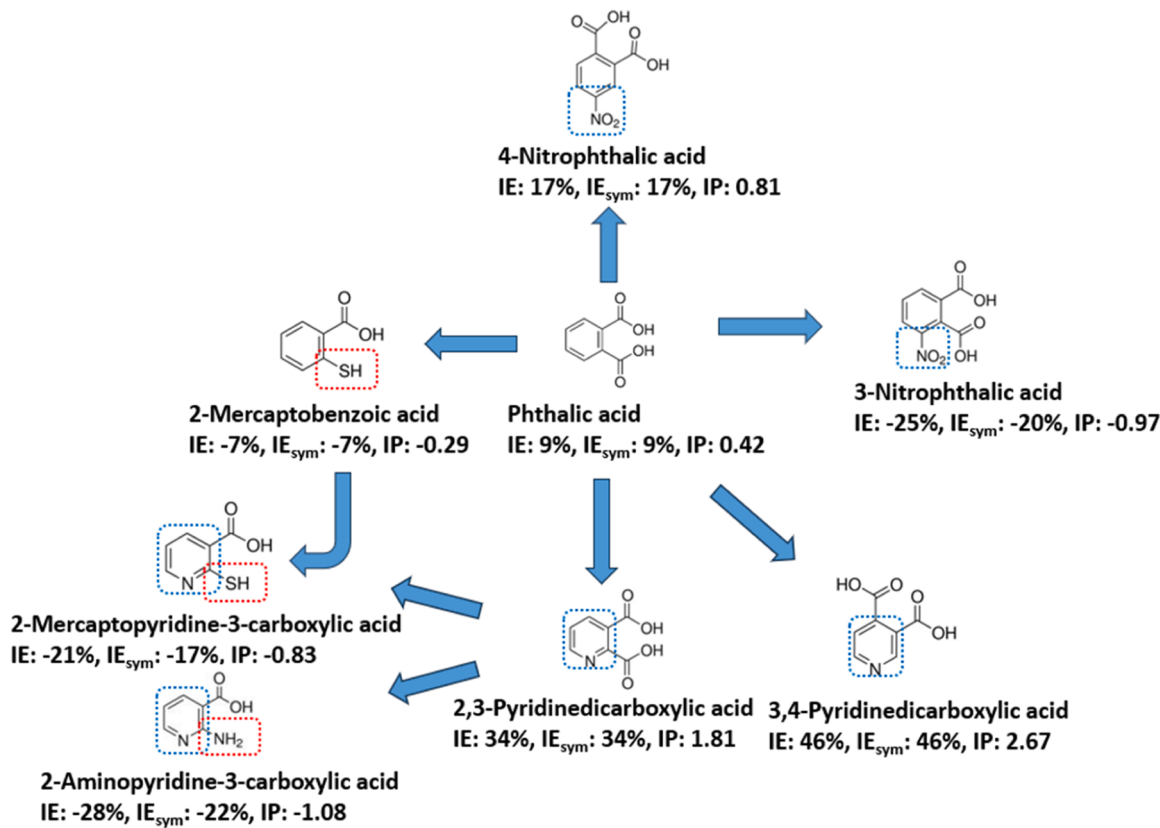


Fig. 7. The molecule structures and inhibition effects of phthalic acid before and after substituted with different functional groups.

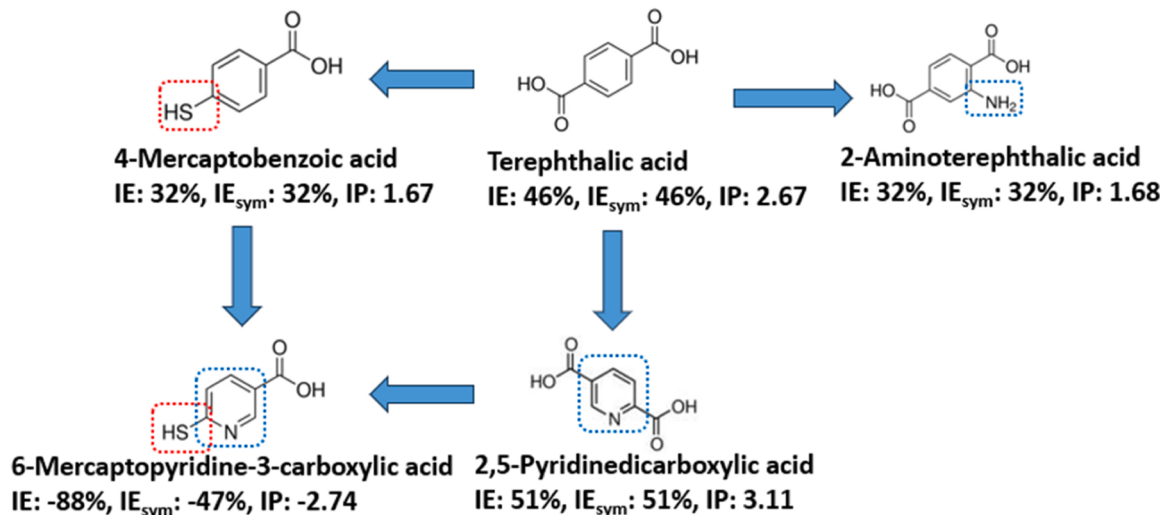
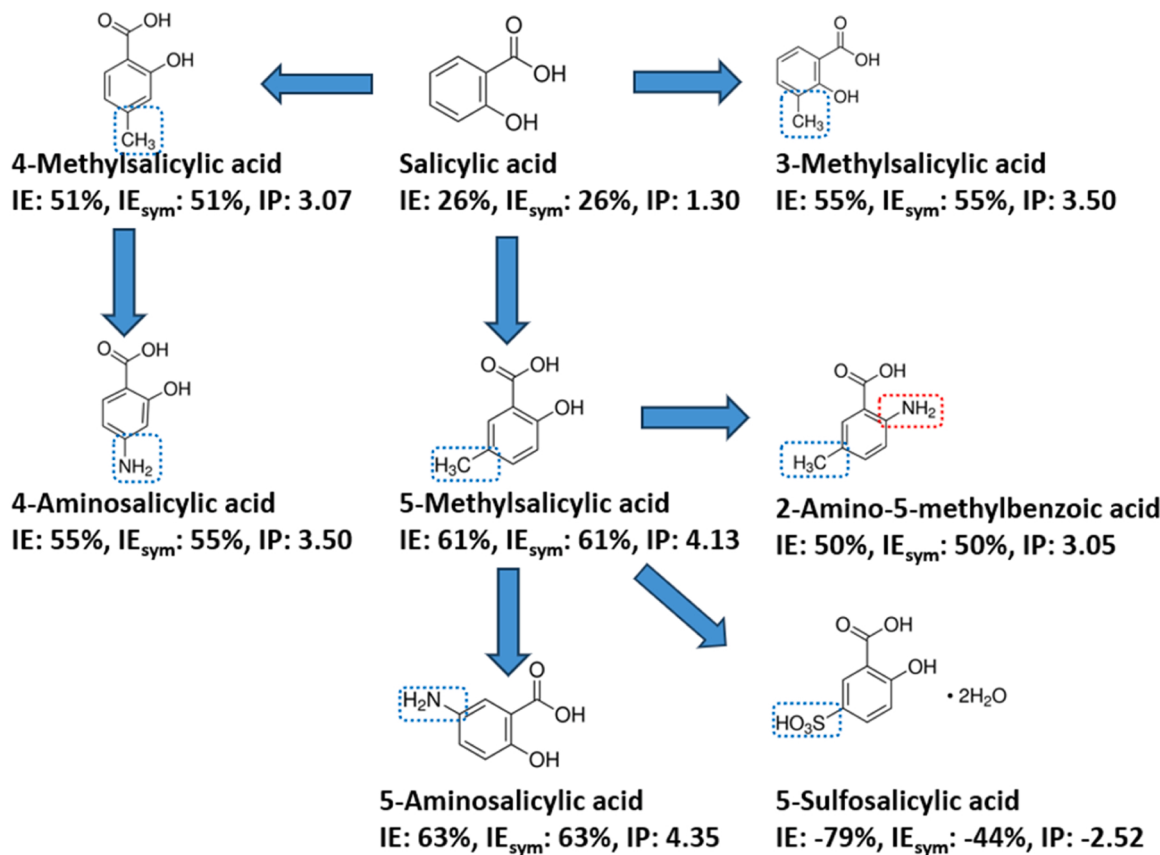


Fig. 8. The molecule structures and inhibition effects of terephthalic acid before and after substituted with different functional groups.

remain similar even higher in some cases. The observed inhibiting effect is likely to be related to their adsorption on the Mg surface by a benzene ring, heterocycle, or monohydroxybenzoic moiety [25,66]. As a comparison, 5-aminoisoquinoline (IE: 62 %, IE<sub>sym</sub>: 62 %, IP: 4.26) shows a high inhibition effect while 8-aminoisoquinoline presents a certain corrosion-accelerating effect. The reason for this phenomenon could be attributed to the adsorption mode of dissolution modulators on the MgO surface [59]: the adsorption of 5-aminoisoquinoline on the AZ31 surface may be arranged in the direction that the benzene ring is horizontal to the Mg surface while the adsorption of 8-aminoisoquinoline might be arranged in the vertical direction considering the positions of

amino-group and the pyridine ring in both dissolution modulators.

Most dissolution modulators containing sulfo-group also accelerate the corrosion of AZ31 alloys. For instance, 8-hydroxy-5-quinoline sulfonic acid (IE: -119 %, IE<sub>sym</sub>: -54 %, and IP: -3.40), 8-hydroxy-7-iodo-5-quinolinesulfonic acid (IE: -56 %, IE<sub>sym</sub>: -36 %, and IP: -3.40), and 5-sulfosalicylic acid (IE: -79 %, IE<sub>sym</sub>: -44 %, and IP: -2.52) demonstrate that the sulfo-group plays an adverse role in AZ31 Mg corrosion. Only one dissolution modulator containing a sulfo-group tested in this study, sodium dodecylbenzene sulfonate (SDBS), seemingly contradicts this observation and presents the second-best inhibition effect (IE: 77 %, IE<sub>sym</sub>: 77 %, and IP: 6.43) in Table S2. A possible explanation for the



**Fig. 9.** The molecule structures and inhibition effects of salicylic acid before and after substituted with different functional groups.

deviation of this dissolution modulator should be similar to aromatic dissolution modulators containing amino-group: the corrosion-accelerating effect of sulfo-group is offset either by the long chain or by a benzene ring.

### 3.3.2. Phosphonate-containing dissolution modulators

A number of phosphonate-containing dissolution modulators have been tested, inspired by recent successful application of selected phosphonates as corrosion inhibitors for Mg and Al alloys [60,61]. As shown in Fig. 4 and Table S2, most phosphonate-containing dissolution modulators shown in this study present a corrosion-accelerating effect. One reason for this behaviour is that dissolution modulators such as ethyl-phosphonic acid ( $pK_{a1}=2.43$ ,  $pK_{a2}=8.05$ ), propylphosphonic acid ( $pK_{a1}=2.49$ ,  $pK_{a2}=8.18$ ), etidronic (hydroxyethylidene-diphosphonic) acid ( $pK_{a1}=1.35$ ,  $pK_{a2}=2.87$ ,  $pK_{a3}=7.03$ ,  $pK_{a4}=11.3$ ), and hypophosphorous acid ( $pK_a=11.1$ ) have high  $pK_a$  values, which buffer the solution pH in this study (initial solution pH is  $7.0 \pm 0.5$ ). Therefore, the solution pH is difficult to achieve the necessary value for the stabilization of  $Mg(OH)_2$  layer on the AZ31 surface. Another reason is that their complexes with  $Mg^{2+}$  may be soluble in aqueous solution. Both reasons lead to the acceleration of Mg dissolution. In contrast, octylphosphonate has a positive inhibition effect because the long-chain structure can result in high hydrophobicity [61]. It is reported that n-octylphosphonate can form self-assembled multilayers on the aluminium oxide surface [62], therefore it can be inferred that a similar mono/multilayer(s) on  $MgO$  surface might be formed.

### 3.3.3. Thiol-containing dissolution modulators

Some thiol-containing dissolution modulators exhibit an inhibition effect on the AZ31 alloy in the results of Fig. 4 and Table S2. Among these, a high inhibition effect is observed for thiourea (IE: 72 %, IE<sub>sym</sub>: 72 %, and IP: 5.60), 3-mercaptopbenzoic acid (IE: 46 %, IE<sub>sym</sub>: 46 %, and

IP: 2.69), heterocyclic thiol: 2,5-thiophenedicarboxylic acid (IE: 74 %, IE<sub>sym</sub>: 74 %, and IP: 5.89), thiadiazoles: 5-amino-1,3,4-thiadiazole-2-thiol (IE: 59 %, IE<sub>sym</sub>: 59 %, and IP: 3.90), and 1,3,4-thiadiazole-2,5-dithiol (IE: 87 %, IE<sub>sym</sub>: 87 %, and IP: 9.02). The inhibition mechanism for thiol-containing compounds on Mg might be related to the suppression of Fe-redeposition, proven to have strong detrimental effect on corrosion of Mg alloys [13]. Mercier et al. [63] reported that sulfur can bind with iron to block the catalytic sites for the HER. It is likely that thiol-containing compounds possess similar Fe and Cu blocking effect suppressing cathodic process on noble impurities. Nevertheless, some thiol-containing dissolution modulators show a low/non-inhibiting effect on the AZ31 alloy.

2-mercaptopbenzoic acid (IE: -7 %, IE<sub>sym</sub>: -7 %, and IP: -0.29) and 4-mercaptopbenzoic acid (IE: 32 %, IE<sub>sym</sub>: 32 %, and IP: 1.67) present a lower inhibition effect than 3-mercaptopbenzoic acid (IE: 46 %, IE<sub>sym</sub>: 46 %, and IP: 2.69). Due to the Fe and Cu blocking effect of the thiol-group [63], it can be deduced that the ortho- (4-mercaptopbenzoic acid) and para- (2-mercaptopbenzoic acid) positions of the thiol- and carboxylate-groups are not beneficial to the combination of mercaptobenzoates and  $Fe^{2+/3+}/Cu^{2+}$ , compared to the meta-position (3-mercaptopbenzoic acid) of thiol- and carboxylate-groups. Furthermore, as shown in Fig. 7 and Fig. 8, after the benzene ring is replaced by a pyridine ring, dissolution modulators with similar structures even show a corrosion-accelerating effect: 6-mercaptopypyridine-3-carboxylic acid (IE: -88 %, IE<sub>sym</sub>: -47 %, and IP: -2.74) and 2-mercaptopypyridine-3-carboxylic acid (IE: -21 %, IE<sub>sym</sub>: -17 %, and IP: -0.83). The possible reason for this phenomenon should be attributed to the complex formation between pyridine ring with  $Mg^{2+}$  [59], which cause the dissolution of Mg but the formed complexation cannot precipitate on the AZ31 surface.

Several pyrimidinethiols, imidazole thiols, and one triazolothiophenol have been tested in this study: 4-amino-6-mercaptopypyrazolo[3,4-d]pyrimidine (IE: 40 %, IE<sub>sym</sub>: 40 %, and IP: 2.20), 4,5-diamino-2,6-

dimercaptopyrimidine (IE: 36 %, IE<sub>sym</sub>: 36 %, and IP: 1.96), 4,6-diamino-2-pyrimidinethiol (IE: 28 %, IE<sub>sym</sub>: 28 %, and IP: 1.44), 2-mercapto-5-methylbenzimidazole (IE: 43 %, IE<sub>sym</sub>: 43 %, and IP: 2.48), 2-mercapto-1-methylimidazole (IE: -35 %, IE<sub>sym</sub>: -26 %, and IP: -1.32), 2-mercaptoimidazole (IE: -5 %, IE<sub>sym</sub>: -5 %, and IP: -0.20), and 4-amino-3-hydrazino-5-mercaptop-1,2,4-triazole (IE: 32 %, IE<sub>sym</sub>: 32 %, and IP: 1.66). These several dissolution modulators contain both amino- and thiol-groups. It has been mentioned in Section 3.3.1 that amino-groups present a corrosion-accelerating effect on the AZ31 alloy in most cases. Therefore, although the detailed inhibition mechanisms of these amino- and thiol-containing dissolution modulators are still unrevealed, it can be inferred that the thiol-group in their structure plays a positive role to prevent corrosion of AZ31 alloy.

### 3.3.4. Carboxyl-containing dissolution modulators

It has been shown that pyridinedicarboxylates (PDCs) (2,3-PDC, 2,5-PDC, 2,6-PDC, and 3,4-PDC) inhibit corrosion of Mg alloys to some degree [59,64]. It is reported that PDCs can form rather strong chelates with Fe<sup>2+/3+</sup> and weak complexes with Mg<sup>2+</sup> to prevent the re-plating of iron and decrease Mg corrosion [13,65]. Song et al. reported 2,6-PDC can form weak complexes with Mg<sup>2+</sup>, decreasing the concentration of free Mg<sup>2+</sup> to form Mg(OH)<sub>2</sub> and delaying the formation of Mg(OH)<sub>2</sub> on the pH scale [64]. Therefore, a denser and more protective Mg(OH)<sub>2</sub> layer on the Mg surface is formed that prevents further corrosion [64]. In the current work, as shown in Table S2 and Fig. 4, the inhibition effects of 2,3-PDC (IE: 34 %, IE<sub>sym</sub>: 34 %, and IP: 1.81) 2,5-PDC (IE: 51 %, IE<sub>sym</sub>: 51 %, and IP: 3.11), 2,6-PDC (IE: 33 %, IE<sub>sym</sub>: 33 %, and IP: 1.71), and 3,4-PDC (IE: 46 %, IE<sub>sym</sub>: 46 %, and IP: 2.67) are lower but still in line with the results reported in previous studies. Additionally, nitrogen- or methyl-substituted salicylates (3-methylsalicylic acid (IE: 55 %, IE<sub>sym</sub>: 55 %, and IP: 3.50), 4-methylsalicylic acid (IE: 51 %, IE<sub>sym</sub>: 51 %, and IP: 3.07), 5-methylsalicylic acid (IE: 61 %, IE<sub>sym</sub>: 61 %, and IP: 4.13), 4-aminosalicylic acid (IE: 55 %, IE<sub>sym</sub>: 55 %, and IP: 3.50) and 5-aminosalicylic acid (IE: 63 %, IE<sub>sym</sub>: 63 %, and IP: 4.35)) also present positive IE values similar to those previously reported in [13].

For aluminium alloys 2024 and 7075, it was reported that ortho- and para-positions of the carboxylate-groups substituted on the pyridine ring are more favourable for corrosion inhibition than the meta-position [66]. This correlates with the field effect of the carboxylate-group whose electron-donating effect would be maximized at ortho- and para- positions [66]. However, for the AZ31 alloy, the inhibition effect of 2,5-PDC is better than that of 2,6-PDC, demonstrating that the inhibition mechanism on Mg is different than on aluminium with respect to the carboxylate position. This can be explained by the steric hindrance effect of carboxylate: the big size of carboxylate hinders the chelation of other carboxylate-groups and adjacent N atoms with Mg<sup>2+</sup> or noble cations such as Fe<sup>2+/3+</sup>. Additionally, the number of carboxylate-groups on the phenyl ring correlates with IE in a certain degree: 23 % for benzoic acid (mono-carboxylic), 46 % for terephthalic acid (1,4-benzenedicarboxylic acid), 9 % for phthalic acid (1,2-benzenedicarboxylic acid), 49 % for trimesic acid (1,3,5-benzenetricarboxylic acid), 32 % for 1,2,3-benzenetricarboxylic acid, 53 % for 1,2,4,5-benzenetetracarboxylic acid, and 19 % for mellitic acid. Establishing structure-property relationships and increasing the understanding of underlying inhibition mechanisms of aromatic carboxylates will be the topic of a follow-up publication.

## 3.4. Validation of profilometer approach

### 3.4.1. Calculation of weight loss

According to the ASTM G1-03 standard chromic acid is used to remove the corrosion products from Mg alloys [67]. This implies full passivation of Mg by chromic acid treatment. However, minor acid etching still causes slight weight loss during chromic acid cleaning, even when applied to the uncorroded Mg surface. This can be neglected when the corrosion impact is high and the loss of uncorroded Mg caused by

chromic acid etching is in relation comparably low (lower than 5 %). However, given that the values of weight loss during the experiments presented in this study are low (milligram range), the material loss caused by chromic acid needs to be accounted for.

Assuming uniform etching by chromic acid across the entire surface of the Mg strip, the gravimetric weight loss caused by chromic acid on area not exposed to the corrosion test solution ( $G_{CA}$  unexposed) can be calculated using Eq. 10.

$$G_{CA \text{ unexposed}} = G_{CA} \frac{S_1 - S_2}{S_1} \quad (10)$$

where  $G_{CA}$  is the balance-measured gravimetric weight loss of one reference Mg strip (with dimension of 80 mm × 15 mm × 2 mm) that was exposed to chromic acid,  $S_1$  is the surface area of one sample (27.8 cm<sup>2</sup>), and  $S_2$  is the total surface area of four corrosion marks on one sample (3.14 cm<sup>2</sup>). Table 1 summarizes the abbreviations and meanings used in this study for the convenience of readers. To obtain an average  $G_{CA}$  unexposed value consistent with the experimental situation, two groups (totalling 12 strips) of Mg samples without exposure to dissolution modulators were cleaned by chromic acid for five minutes. The gravimetric weight loss due to chromic acid etching ( $G_{CA}$ ) was then measured using a balance. Table 2 shows the calculated results of  $G_{CA}$  unexposed for 12 reference samples and their average value was found to be 0.51 mg. Therefore,  $G$ , the balance-measured gravimetric weight loss of a sample exposed to a dissolution modulator (four corrosion marks in one Mg strip) can be calculated using Eq. 11.

$$G = G_{total} - G_{CA \text{ unexposed}} \quad (11)$$

where  $G_{total}$  is the total gravimetric weight loss of a strip measured by the balance, which includes the weight loss caused by the exposure of dissolution modulators and chromic acid cleaning. It should be noted that the  $G_{CA}$  unexposed value for each specific reference sample is different, from 0.1 mg to 0.8 mg. Given that such variances may also occur for other experimental samples, the final  $G$  results might differ from the weight loss caused by the exposure of dissolution modulators.

### 3.4.2. Processing of profilometric weight loss and balance-measured weight loss

The values of  $P$ ,  $G$  and the ratio of  $P$  to  $G$  are presented in Table 3. Each result represents the sum of four marks for each sample. Since there are several strips in different groups tested with NaCl blank solution, the

**Table 1**  
Abbreviations and their meanings present in this study.

Abbreviations	Meaning
IE	Inhibition efficiency
IP	Inhibition power
IE <sub>sym</sub>	Symmetrized inhibition efficiency
WL	Weight loss caused by corrosion
P(V)	Profilometer measured (profilometric) volume loss caused by the corrosion due to the exposure into 3.5 wt% NaCl solution or containing dissolution modulator
P	Profilometer measured (profilometric) weight loss caused by the corrosion due to the exposure into 3.5 wt% NaCl solution containing dissolution modulator
G	The weight loss as measured by gravimetry for one Mg stripe (80 mm × 15 mm × 2 mm) caused by the corrosion due to the exposure into 3.5 wt% NaCl solution or containing dissolution modulators
$G_{CA}$	Without exposure, the weight loss as measured by gravimetry for one Mg stripe (80 mm × 15 mm × 2 mm) caused by the etching due to chromic acid cleaning.
$G_{total}$	The total weight loss as measured by gravimetry for one Mg stripe (80 mm × 15 mm × 2 mm), which includes $G$ and $G_{CA}$ .
$G_{CA \text{ unexposed}}$	The weight loss as measured by gravimetry for one Mg stripe (80 mm × 15 mm × 2 mm) caused by the etching due to chromic acid cleaning on the area unexposed to 3.5 wt% NaCl solution or containing dissolution modulators

**Table 2**

$G_{CA}$  and  $G_{CA\ unexposed}$  values for 12 reference samples.  $G_{CA}$ : without exposure, the weight loss as measured by gravimetry for one reference Mg stripe caused by the etching due to chromic acid cleaning.  $G_{CA\ unexposed}$ : the weight loss as measured by gravimetry for one Mg strip caused by the etching due to chromic acid cleaning on the area not exposed to 3.5 wt% NaCl solution or containing dissolution modulators.

Reference sample	#1	#2	#3	#4	#5	#6	#7	#8	#9	#10	#11	#12	Ave.
$G_{CA}$ (mg)	0.5	0.7	0.6	0.4	0.1	0.7	0.8	0.7	0.8	0.5	0.5	0.7	$0.58 \pm 0.20$
$G_{CA\ unexposed}$ (mg)	0.44	0.62	0.53	0.35	0.09	0.62	0.71	0.62	0.71	0.44	0.44	0.62	$0.51 \pm 0.18$

**Table 3**

Profilometric weight loss (P), gravimetric weight loss (G) after exposure to 3.5 wt% NaCl solution or containing dissolution modulators, and the ratio between P and G.

Sample number	Dissolution modulator	P (mg)	G (mg)	P/G (%)	Pitting factor
1-1	Benzotriazole	4.08	4.8	85	30.00 ± 6.96
1-2	3,5-Dimethylpyrazole	2.43	2.5	98	19.11 ± 5.94
1-3	1,2,4-Triazole	7.51	7.8	96	17.90 ± 5.36
1-4	Hexamethylenetetramine	2.99	3.2	94	20.28 ± 4.75
1-5	5,5-Dimethylhydantoin	8.08	9.1	89	18.71 ± 1.18
1-6	NaCl	1.96	2.7	73	21.01 ± 5.60
2-1	Piperazine	4.06	5.2	78	17.42 ± 3.50
2-2	4-Isopropylbenzoic acid	2.62	2.8	94	21.71 ± 7.51
2-3	4-Tert-butylbenzoic acid	3.03	2.6	117	24.99 ± 7.29
2-4	3-Methyl-2-nitrobenzoic acid	10.55	11.8	89	6.81 ± 1.66
2-5	NaCl	3.03	3.4	89	15.40 ± 3.41
3-1	2'-Hydroxy-4'-methoxyaceto-phenone	1.53	2.1	73	21.62 ± 3.06
3-2	Mandelic acid	1.79	1.9	95	25.74 ± 5.81
3-3	1-Pheny-1,3-butanedione	2.12	1.9	112	26.58 ± 9.23
3-4	Maltol	5.09	5.6	91	20.44 ± 15.62
3-5	Glycolic acid	1.35	1.6	85	31.21 ± 3.39
3-6	NaCl	2.00	2.7	74	24.94 ± 6.11
4-1	Oxalic acid	1.42	1.0	143	20.14 ± 3.35
4-2	Lactic acid	3.29	3.0	110	23.01 ± 7.32
4-3	Maleic acid	2.10	2.6	81	14.92 ± 2.96
4-4	Malonic acid	1.98	1.9	105	18.82 ± 4.65
4-5	Succinic acid	2.23	2.1	107	22.67 ± 6.84
4-6	NaCl	2.09	3.0	70	23.54 ± 3.40
5-1	Alginic acid sodium salt from brown algae	1.38	1.6	87	43.30 ± 5.95
5-2	Chitosan	1.91	2.5	77	23.60 ± 6.26
5-3	Dextran	1.72	2.0	86	25.43 ± 1.69
5-4	Penicillin G Na salt	3.25	3.9	84	40.44 ± 2.41
5-5	Folic acid	2.41	3.0	81	23.03 ± 7.27
5-6	NaCl	2.34	2.5	94	23.58 ± 4.48
Ave.				92	
STDEV				16	

strips are numbered to differentiate them. For example, the label 1–2 refers the second sample of the first group. From these results, it is clearly seen that P values for most samples are slightly lower than G where the average value of P/G is 0.92 with a StDev of 0.16.

The comparison between profilometric and balance-measured weight loss is presented in Table 4. IE-G, IE-P,  $IE_{sym}$ -G,  $IE_{sym}$ -P, IP-G, and IP-P are shown for five experimental batches, including a total of 25 randomly selected dissolution modulators. As mentioned before, the IE,  $IE_{sym}$ , and IP calculated by P are referred to as IE-P,  $IE_{sym}$ -P, and IP-P, respectively. The IE,  $IE_{sym}$ , and IP calculated by G are denoted as IE-G,  $IE_{sym}$ -G, and IP-G, respectively. Accordingly, the relationships between the values obtained by topography and gravimetry are plotted in Fig. 10 a, b and c. The absolute residual values ( $|\sigma|$ ) between  $IE_{sym}$ -P and  $IE_{sym}$ -G, denoted as  $|\sigma|$  ( $IE_{sym}$ -P,  $IE_{sym}$ -G), are displayed in Fig. 10 d, which is calculated by Eq. 12. Through this figure, the differences between their  $IE_{sym}$ -P values and  $IE_{sym}$ -G values can be revealed systematically.

$$|\sigma| = |IE_{sym}\text{-}P - IE_{sym}\text{-}G| \quad (12)$$

It is clearly seen that for three metrics reflecting the inhibition effect, profilometric values correlate well with those measured by balance. However, all linear regression lines for these three metrics are below the line for perfect agreement, indicating that P is lower than G in most cases. The data points for  $IE_{sym}$  and IP are uniformly distributed over the entire range of the X and Y axis, while most IE data points are clustered in the upper right (between –50–50) and are hard to differentiate visually (Fig. 10 a). This is mainly related to the aforementioned nonlinearity of IE, whereas IP and  $IE_{sym}$  rank dissolution modulators in a less imbalanced way, regardless of whether they are inhibitors or accelerators [25,26]. Meanwhile, the  $|\sigma|$  (Fig. 10 d) is higher as  $IE_{sym}$ -G increases. This suggests the profilometric method can reveal dissolution modulators with corrosion-accelerating effects better than those with positive inhibition effects in the case of  $IE_{sym}$ . Although the slope of IE (Fig. 10 a) is higher than 1.00, which can lead to a different conclusion from  $IE_{sym}$  and IP, given that most points of dissolution modulators are clustered together, the analysis of the slope for IE is less convincing compared with  $IE_{sym}$  and IP. Overall, it is confirmed that topographic measurements provide reliable data for screening the corrosion inhibition effect of multiple dissolution modulators on Mg alloys.

### 3.5. The limitations of the profilometer approach

Based on the data presented in Fig. 10, Table 3, and Table 4, the volume loss results acquired by topographical scanning of the corroded surface are a good fit for the weight loss results measured by the analytical balance. Nevertheless, there is still a discrepancy for certain dissolution modulators when comparing the absolute values of the weight loss provided by topographic versus gravimetric measurements. In this part, the causes are analysed by observing the plane and cross-section views of the corrosion marks by SEM.

As discussed above, the average value of P/G is  $0.92 \pm 0.16$ , demonstrating that profilometer correlates well with the balance-measured weight loss results. However, the values of P/G are higher or lower than 1.0 for certain dissolution modulators, as presented in Table 3. In order to explore the reason behind this phenomenon, cross-section observations of similar positions produced by SEM and profilometer were made. It should be pointed out that the correlation between the topographic profiles and SEM cross-sections described below was

**Table 4**

Inhibition efficiency, inhibition power, and symmetrized inhibition efficiency calculated by gravimetric weight loss (IE-G, IE<sub>sym</sub>-G, and IP-G) after exposure to 3.5 wt % NaCl solution containing dissolution modulators and corresponding metrics values calculated based on profilometric weight loss (IE-P, IE<sub>sym</sub>-P, and IP-P).

Sample number	Dissolution modulator	IE-G (%)	IE-P (%)	IE <sub>sym</sub> -G (%)	IE <sub>sym</sub> -P (%)	IP-G	IP-P
1-1	Benzotriazole	-78	-107	-44	-52	-2.50	-3.17
1-2	3,5-Dimethylpyrazole	7	-24	7	-19	0.33	-0.93
1-3	1,2,4-Triazole	-189	-283	-65	-74	-4.61	-5.83
1-4	Hexamethyleneteramine	-19	-52	-16	-34	-0.74	-1.82
1-5	5,5-Dimethylhydantoin	-237	-312	-70	-76	-5.28	-6.15
2-1	Piperazine	-53	-34	-35	-25	-1.85	-1.27
2-2	4-Isopropylbenzoic acid	18	14	18	14	0.84	0.64
2-3	4-Tert-butylbenzoic acid	24	0	24	0	1.17	0
2-4	3-Methyl-2-nitrobenzoic acid	-247	-248	-71	-71	-5.40	-5.42
3-1	2'-Hydroxy-4'-methoxyacetophenone	22	23	22	23	1.07	1.16
3-2	Mandelic acid	30	11	30	11	1.53	0.49
3-3	1-Pheny-1,3-butanedione	30	-6	30	-6	1.53	-0.26
3-4	Maltol	-107	-155	-52	-61	-3.17	-4.06
3-5	Glycolic acid	41	33	41	33	2.27	1.71
4-1	Oxalic acid	67	32	67	32	4.77	1.67
4-2	Lactic acid	0	-57	0	-36	0.00	-1.97
4-3	Maleic acid	13	-1	13	-1	0.62	-0.02
4-4	Malonic acid	37	5	37	5	1.98	0.24
4-5	Succinic acid	30	-7	30	-6	1.55	-0.28
5-1	Alginic acid sodium salt from brown algae	36	41	36	41	1.94	2.27
5-2	Chitosan	0	18	0	18	0.00	0.88
5-3	Dextran	20	26	20	26	0.97	1.32
5-4	Penicillin G Na salt	-56	-39	-36	-28	-1.93	-1.44
5-5	Folic acid	-20	-3	-17	-3	-0.79	-0.14

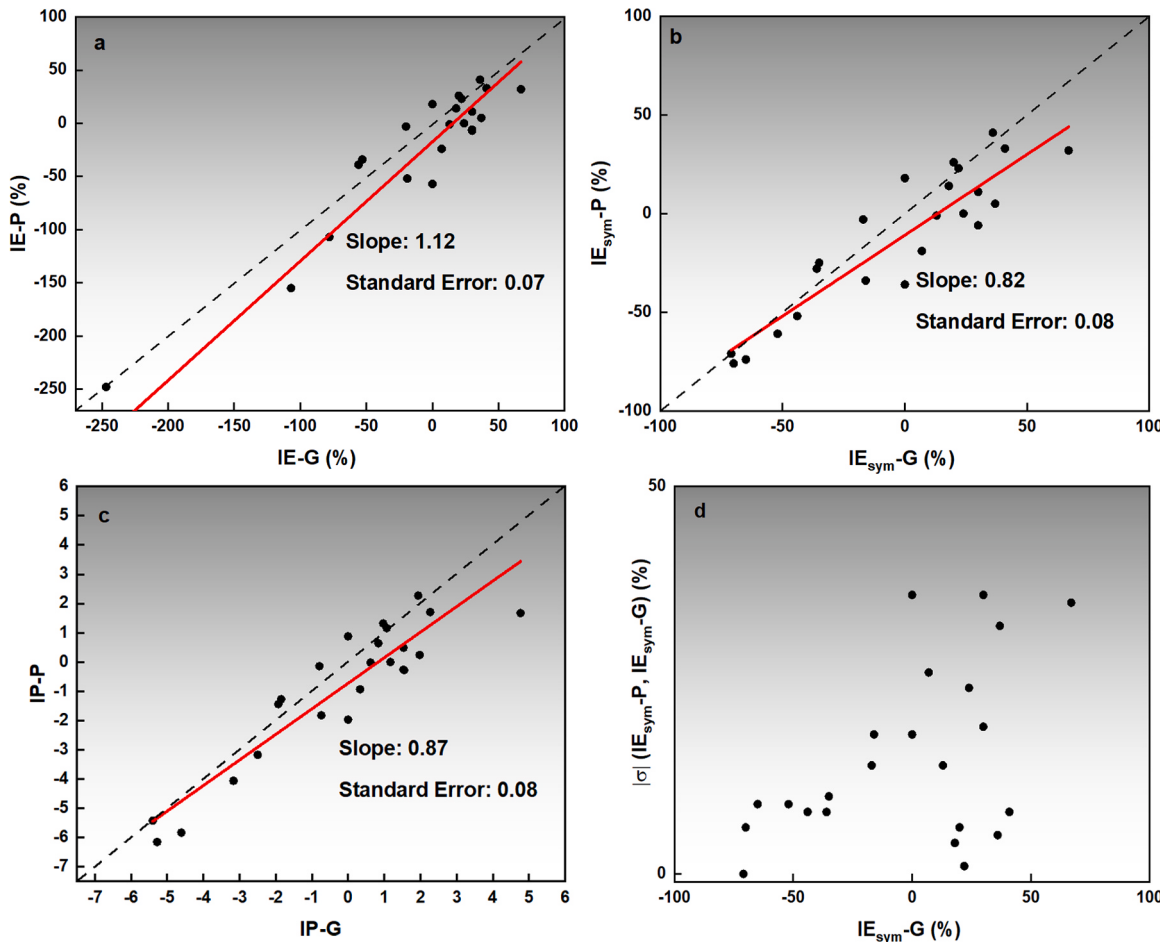


**Fig. 10.** Relationship between profilometric weight loss (P) and gravimetric weight loss (G): **a** inhibition efficiency (IE); **b** symmetrized inhibition efficiency (IE<sub>sym</sub>); **c** inhibition power (IP). **d** absolute residual ( $|\sigma|$ ) between IE<sub>sym</sub>-P and IE<sub>sym</sub>-G.

performed manually and is not devoid of deviation at the microscopic level.

The topographic quantification underestimated the amount of Mg removed by corrosion exposure in blank NaCl solution (Table 3, sample 1–6, P/G = 0.73). The corresponding cross-sections are shown in Fig. 11. By comparing the profilometric profile curve with an SEM cross-section micrograph, the similar position shown in SEM morphology could be found in the profilometer software. In Fig. 11 c and d, the blue dashed lines represent the profile curves shown in Fig. 11 a and b, superimposed on the SEM cross-sections. It can be observed that the blue dashed line matches the profile of the corroded sample fairly well in both images (Fig. 11 c and d), confirming the positions found by both techniques are similar. However, zooming into a part of the SEM cross-section (Fig. 11 d), it can be found that the corroded surface is rather rough while the profile curve produced by profilometer is a smooth line, suggesting some detailed information cannot be detected by profilometer. The X-Y (lateral) resolution of the profilometer at magnification 40 × is 7.4 μm. Fig. 11 g and h show that a typical localized corrosion produces a morphology with the diameters of many corrosion holes lower than 7.4

μm. Therefore, it could be inferred that these small diameter corrosion pits will be the blind areas and cannot be detected because either the resolution is not sufficiently high, or the corroded area is masked by other uncorroded area from the profilometer view. Additionally, even though one cavity, marked as position A in Fig. 11 d, is about 45 μm in diameter, it is still underestimated by profilometer, which may be attributed to the profile smoothing processing by the profilometer at 40-fold magnification. To further confirm this assumption, higher magnification lenses (80 × and 120 ×) were used. Corresponding profiles are overlapped with the corresponding SEM displayed in Fig. 11 e and f. Compared to the profilometric profile at 40-fold magnification, these two profiles exhibit more detailed information. For instance, the corrosion pit at position A is detected at these two higher magnifications. After a series of data processing, the P/G values of sample (1–6) are 1.04 (P: 2.82 mg, 80 seconds) at 80-fold magnification and 1.06 (P: 2.85 mg, 160 seconds) at 120-fold magnification, which is higher than the P/G (0.73) and P (1.96 mg, 30 seconds) measured at 40-fold magnification. Given that the X-Y resolutions of the profilometer at 80-fold and 120-fold magnification are 3.7 μm and 2.1 μm respectively,

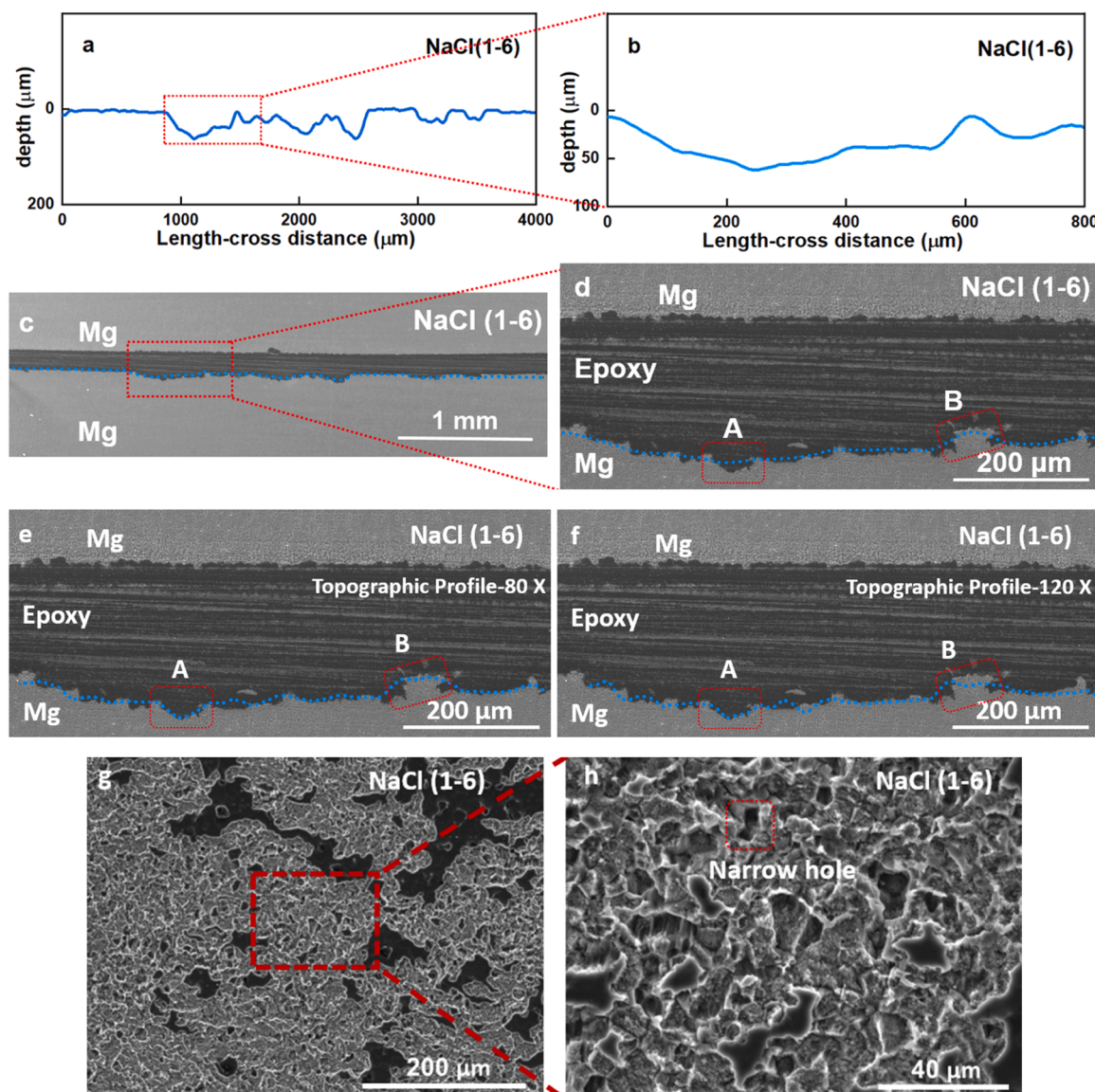


**Fig. 11.** a Profilometric cross-section of the sample 1–6; c SEM cross-section micrographs of the same position as a; b and d are higher magnifications for a and c; the x-axis distance of the zoom out micrograph shown in a and c is the same (4000 μm); e and f are the same SEM micrographs as shown in d but topography was mapped with different lenses (magnification 80 × and 120 ×); g and h are top view SEM micrographs of the same sample; the x-axis distance of the micrograph shown in b, d, e, and f is same (800 μm).

it could be concluded that the insufficient resolution actually leads to lower topographic recovery. Since the resolution in Z-direction decreases as the magnification increases, the main advantage of using lower magnification remains as a higher Z resolution can be ensured. Besides, the most efficient inhibitors are not expected to induce localized corrosion that is difficult to uncover by profilometric analysis. Meanwhile, position B marked in Fig. 11 d, e and f shows the overestimation of the profile compared to the SEM cross-section, which also originates from the inadequate resolution and the smoothing process of the profilometer.

From the discussion above, it can be concluded that the morphology of corrosion localization affects the accuracy of topographic measurements: a relatively flat surface improves the topographic accuracy, while the rough surface causes over- or underestimation of topographic mapping due to the inadequate resolution of the profilometer and the profile smoothening.

The topographic quantification overestimated the amount of Mg removed by corrosion exposure for 4-tert-butylbenzoate (Table 3, sample 2–3, P/G = 1.17). Fig. 12 a is the topographic profile and Fig. 12 b is the corresponding SEM cross-section micrograph. From Fig. 12 b, this sample exhibits some extent of localized corrosion. It can be seen that there is a good match between the SEM cross-section and the topographic profile obtained by the profilometric method, although slightly underestimations of corrosion pits still exist. Nevertheless, most of the Mg removed by corrosion can be detected by profilometric analysis. As shown in Fig. 12 c and d, corrosion leads to some open corrosion pits, which are conducive to accurate topographic results when uncovered. However, based on the above explanation, the P acquired by profilometric analysis should match the G slightly less, instead of being much higher as in this case. A plausible explanation can be a lower-than-average impact of chromic acid used for removing the corrosion products before measuring G. Based on the results in Table 2, the average value of 0.51 mg is subtracted from the balance-measured weight loss to account for the material removed by chromic acid cleaning. If the actual effect of chromic acid was lower in this case, e.g., 0.1 mg like for reference sample #5, this would lead to a G value of 3.0 mg for this sample (2–3) and P/G = 1.01. Therefore, the discrepancy in weight loss etched by chromic acid cleaning will also affect the calculated P/G ratio. This is also the reason for P/G close to 1.00 in terms of sample 2–5 and

5–6, although both samples were tested by blank NaCl solution.

Overall, several factors affect the P/G ratio:

Firstly, some corrosion pits and cavities with small size are ignored by the profilometric analysis because their sizes are lower than the profilometer resolution. Secondly, for the same reason, some small-sized protrusions on the Mg surface cannot be detected by the profilometer either. Both can lead to under- or overestimation of P. Correspondingly, samples with homogeneously corroded surface enable higher recovery of volume loss during topographic scanning and return the values of weight loss closest to those measured by the balance.

Additionally, as shown in Table 2, the  $G_{CA}$  unexposed value should be different for different cases. As discussed earlier, if the weight loss etched by chromic acid of one sample is lower than 0.51 mg, this will lead to a lower G than the actual weight loss when 0.51 mg is used for calculating. The weight loss etched by chromic acid is different for different samples. To give a more intuitive explanation, the influence of using different  $G_{CA}$  unexposed values (from 0.1 to 1.0 mg) on the P/G ratio for the above-mentioned two samples (1–6 and 2–3) has been calculated and listed in Table 5. It is shown that the P/G values vary from 0.63 to 0.89 and 1.01–1.38 for samples 1–6 and 2–3 according to different  $G_{CA}$  unexposed values. Therefore, the average  $G_{CA}$  unexposed of 0.51 mg, is not always correct and will affect the G. These factors indicate that severe corrosion is more convenient to be measured by the profilometric method. Higher weight loss (characteristic for dissolution accelerators) can be recovered more accurately by the profilometric method because higher weight loss should lead to a lower relative error in the gravimetric measurements, since the non-reproducibility effect associated with chromic acid etching will have lower relative contribution to the obtained value of weight loss.

It is worth noting that crevice corrosion might occur in the multi-well setup. Figure S2, presents the optical photographs of 116 corrosion marks for the first five testing groups. Each before and after removing the corrosion products. Only 2 plates, in groups 1–3 (1,2,4-triazole) and 4–3 (maleic acid), have clear marks of crevice corrosion. These samples were also characterized by high extent of overall corrosion attack. Thus, like in many other experimental setups, crevice corrosion might occur and is hard to avoid. Yet, it would more likely occur in presence of weak corrosion inhibitors (of lesser importance as screening output) and does not compromise the accuracy of most of the data points.

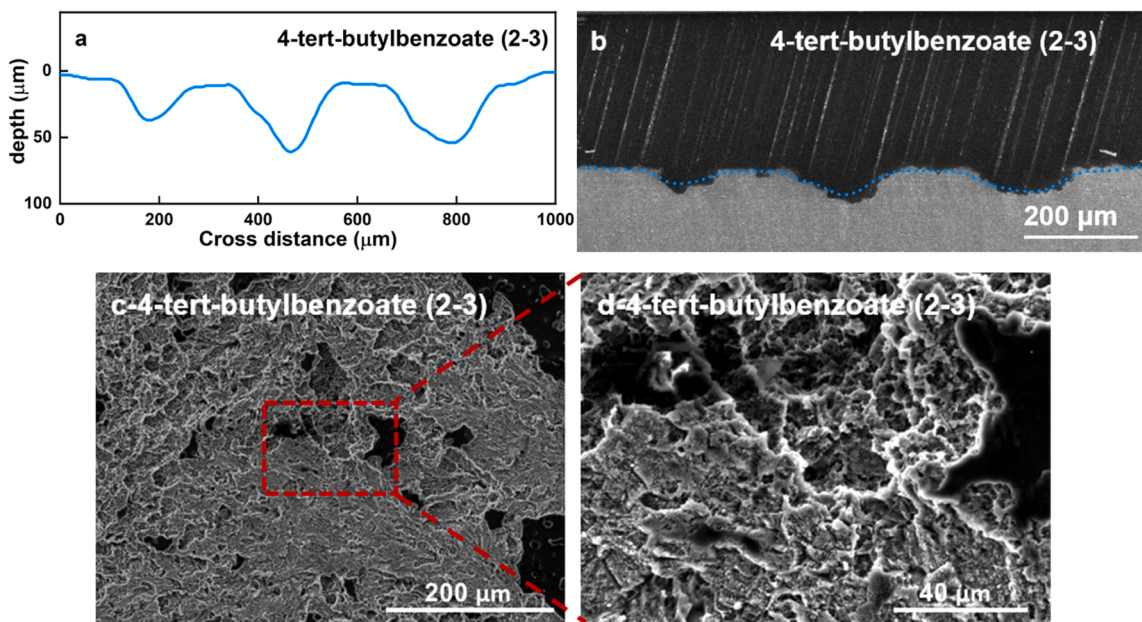


**Fig. 12.** a Cross-section profile of selection area of the sample tested by 4-tert-butylbenzoate (2–3) and the same area observed by SEM; the dotted line in b is the superposition of the profile in a; c and d are the top micrographs of the sample tested by 4-tert-butylbenzoate (2–3).

**Table 5**

P/G values (ratio between profilometric and gravimetric weight loss) for using different  $G_{CA}$  unexposed (gravimetric weight loss caused by chromic acid cleaning on the area unexposed to corrosive solutions) for 1–6 and 2–3 samples.

$G_{CA}$ unexposed (mg)	0.1	0.2	0.3	0.4	0.5	0.6	0.7	0.8	0.9	1.0
1–6	0.63	0.65	0.68	0.70	0.73	0.75	0.78	0.82	0.85	0.89
2–3	1.01	1.04	1.08	1.12	1.17	1.21	1.26	1.32	1.38	1.44

Overall, even with the limitations described above, topographic surface scanning and volume loss quantification show high correlation with direct weight loss measurements. Furthermore, there is a linear relationship between P and G for  $IE_{sym}$  and IP, respectively. Another advantage of profilometric analysis is calculating the pitting factor, which is an important parameter when selecting corrosion inhibitors for industrial applications requiring long-lasting mechanical integrity of metallic parts. Profilometry is able to quantify the volume loss and pitting factor of an individual corroded area. While the traditional gravimetric method is unable to reflect the corrosion localization, the profilometry can quantify the localized distribution of the material loss as a consequence of corrosion attack. As such, profilometric data can be used to assist training an image recognition machine learning model able to estimate the corrosion impact based on an optical image of corroded sample. This will be presented in the follow up publications.

#### 4. Conclusions

A new, larger-than-ever database of dissolution modulators for the magnesium alloy AZ31 is reported here. It includes corrosion inhibition and pitting factor. 229 individual small organic compounds have been tested (mostly in quadruplicate) by the high-throughput multi-well method. The amount of magnesium alloy AZ31 removed by the corrosion exposure was determined by topographical quantification of corrosion marks. The first five groups of tested samples, 25 dissolution modulators in total, including those tested in blank NaCl, in presence of inhibitors, and accelerators were employed to validate the reliability of profilometric measurements. The results were compared with those obtained by traditional gravimetric analysis. Even though there are outliers, there is a high correlation between two groups of experimental results. Therefore, the combination of profilometric quantification with high-throughput corrosion exposure experiment is suited to accelerate exploration of dissolution modulators with respect to Mg corrosion among large number of commercially available compounds. Employing this newly developed approach, the values of pitting factor, inhibition efficiency and two recently introduced alternative metrics, namely inhibition power, and symmetrized inhibition efficiency, were calculated. 1,3,4-thiadiazole-2,5-dithiol (IE: 87 %, IP: 9.02,  $IE_{sym}$ : 87 %, PF: 5.4), sodium dodecylbenzene sulfonate (IE: 77 %, IP: 6.43,  $IE_{sym}$ : 77 %, PF: 37.0), and 2,5-Thiophenedicarboxylate (IE: 74 %, IP: 5.89,  $IE_{sym}$ : 74 %, PF: 32.3) could be identified as the most efficient inhibitors in this study. Moreover, the versatile database will provide the basis for the development of data-driven models to identify corrosion inhibitors causing high IE and low PF values at the same time.

#### CRediT authorship contribution statement

**Zheludkevich Mikhail L.:** Writing – review & editing, Supervision, Conceptualization. **Albarqouni Shadi:** Writing – review & editing, Supervision, Conceptualization. **Nienaber Maria:** Writing – review & editing, Investigation. **Bohlen Jan:** Writing – review & editing, Supervision. **Song Ci:** Writing – review & editing, Writing – original draft, Validation, Investigation, Conceptualization. **Vaghefinazari Bahram:** Writing – review & editing, Investigation. **Feiler Christian:** Writing – review & editing, Supervision, Conceptualization. **Lamaka Sviatlana V.:** Writing – review & editing, Supervision, Conceptualization. **Mei Di:** Writing – review & editing, Investigation. **Wüerger Tim:** Writing – review & editing, Investigation. **Lisitsyna Anna:** Writing – review &

editing, Investigation.

#### Declaration of Competing Interest

The authors declare that they have no known competing financial interests or personal relationships that could have appeared to influence the work reported in this paper.

#### Acknowledgements

This work was supported by AI<sup>2</sup>. Eyesight to AI: Discovery of efficient corrosion modulators via predictive machine learning models, 2020–2023 (Funded by HGF) and Deutsche Forschungsgemeinschaft (DFG, German Research Foundation) – project number 535656357, OPTIMA (Identification of optimal corrosion inhibitors for bare and PEO coated magnesium alloy by combining machine learning and robotic testing). Mr. Ci Song thanks China Scholarship Council for the award of fellowship and funding (No. 202008410217). Dr. Di Mei thanks the National Natural Science Foundation of China (52301107) and the Henan Province high-end Foreign Experts Introduction Program (HNGD2022037). The authors would like to acknowledge Prof. Benjamin Klusemann for providing the access to the profilometer, Keyence VR-5000. The authors would like to acknowledge the technical support from Ms. Petra Fischer and Mr. Gert Wiese.

#### Appendix A. Supporting information

Supplementary data associated with this article can be found in the online version at doi:10.1016/j.corsci.2025.112903.

#### Data availability

Data will be made available on request.

#### References

- [1] M. Esmaily, J.E. Svensson, S. Fajardo, N. Birbilis, G.S. Frankel, S. Virtanen, R. Arrabal, S. Thomas, L.G. Johansson, Fundamentals and advances in magnesium alloy corrosion, *Prog. Mater. Sci.* 89 (2017) 92–193.
- [2] A. Atrens, X. Chen, Z. Shi, Mg corrosion-recent progress, *Corros. Mater. Degrad.* 3 (2022) 566–597.
- [3] Y. Huang, Y. Zhang, J. Song, F. Pan, R. Willumeit-Römer, K.U. Kainer, N. Hirt, Development and prospects of degradable magnesium alloys for structural and functional applications in the fields of environment and energy, *J. Magnes. Alloy.* 11 (2023) 3926–3947.
- [4] J. Bai, Y. Yang, C. Wen, J. Chen, G. Zhou, B. Jiang, X. Peng, F. Pan, Applications of magnesium alloys for aerospace: a review, *J. Magnes. Alloy.* 11 (2023) 3609–3619.
- [5] J. Zhang, J. Miao, N. Balasubramani, D.H. Cho, T. Avey, C.-Y. Chang, A.A. Luo, Magnesium research and applications: past, present and future, *J. Magnes. Alloy.* 11 (2023) 3867–3895.
- [6] K. Gusieva, C.H.J. Davies, J.R. Scully, N. Birbilis, Corrosion of magnesium alloys: the role of alloying, *Int. Mater. Rev.* 60 (2015) 169–194.
- [7] W. Ci, X. Chen, X. Dai, C. Liu, Y. Ma, D. Zhao, F. Pan, Achieving ultra-high corrosion-resistant Mg-Zn-Sc alloys by forming Sc-assisted protective corrosion product film, *J. Mater. Sci. Technol.* 181 (2024) 138–151.
- [8] W. Ci, X. Chen, Y. Sun, X. Dai, G. Zhu, D. Zhao, F. Pan, Effect of Zn on mechanical and corrosion properties of Mg-Sc-Zn alloys, *J. Mater. Sci. Technol.* 158 (2023) 31–42.
- [9] H. Hornberger, S. Virtanen, A.R. Boccaccini, Biomedical coatings on magnesium alloys - a review, *Acta Biomater.* 8 (2012) 2442–2455.
- [10] D. Zhang, F. Peng, X. Liu, Protection of magnesium alloys: from physical barrier coating to smart self-healing coating, *J. Alloy. Compd.* (2021) 853.
- [11] C. Wang, J. Shen, F. Xie, B. Duan, X. Xie, A versatile dopamine-induced intermediate layer for polyether imides (PEI) deposition on magnesium to render robust and high inhibition performance, *Corros. Sci.* 122 (2017) 32–40.

- [12] Y.-X. Yang, Z. Fang, Y.-H. Liu, Y.-C. Hou, L.-G. Wang, Y.-F. Zhou, S.-J. Zhu, R.-C. Zeng, Y.-F. Zheng, S.-K. Guan, Biodegradation, biocompatibility and covalent bonding mechanism of electrografting polyethylacrylate coating on Mg alloy for cardiovascular stent, *J. Mater. Sci. Technol.* 46 (2020) 114–126.
- [13] S.V. Lamaka, B. Vaghefinazari, D. Mei, R.P. Petruskas, D. Höche, M. L. Zheludkevich, Comprehensive screening of Mg corrosion inhibitors, *Corros. Sci.* 128 (2017) 224–240.
- [14] X.P. Guo, G.L. Song, J.Y. Hu, D.B. Huang, Corrosion inhibition of magnesium (Mg) Alloys, : *Corros. Prev. Magnes. Alloy.* (2013) 61–84.
- [15] L. Ma, W. Li, S. Zhu, L. Wang, S. Guan, Corrosion inhibition of Schiff bases for Mg-Zn-Y-Nd alloy in normal saline: experimental and theoretical investigations, *Corros. Sci.* (2021) 184.
- [16] D.A. Winkler, A.E. Hughes, C. Özkan, A. Mol, T. Würger, C. Feiler, D. Zhang, S. V. Lamaka, Impact of inhibition mechanisms, automation, and computational models on the discovery of organic corrosion inhibitors, *Prog. Mater. Sci.* 149 (2025).
- [17] S.P. den Braver-Sewradj, J. van Benthem, Y.C.M. Staal, J. Ezendam, A.H. Piersma, E.V.S. Hessel, Occupational exposure to hexavalent chromium. Part II. Hazard assessment of carcinogenic effects, *Regul. Toxicol. Pharmacol.* 126 (2021) 105045.
- [18] Y. Zhou, S. Zanna, A. Seyeux, L. Wang, P. Marcus, J. Świątowska, Influence of sodium 5-sulfosalicylate as a corrosion inhibitor in NaCl electrolyte on enhanced performances of Mg-air batteries, *Electrochim. Acta* 435 (2022) 141360.
- [19] H. Pulikalparambil, S. Siengchin, J. Parameswaranpillai, Corrosion protective self-healing epoxy resin coatings based on inhibitor and polymeric healing agents encapsulated in organic and inorganic micro and nanocontainers, *Nano-Struct. Nano-Objects* 16 (2018) 381–395.
- [20] Y. Wu, L. Wu, W. Yao, Y. Chen, Y. Zhou, L. Wang, T. Wu, B. Jiang, A. Atrens, F. Pan, ZnAl-LDH@MXene modified by inhibitor as a nanofiller applied on Mg alloys coating protection, *Carbon* 204 (2023) 36–49.
- [21] G. Zhang, E. Jiang, L. Wu, W. Ma, H. Yang, A. Tang, F. Pan, Corrosion protection properties of different inhibitors containing PEO/LDHs composite coating on magnesium alloy AZ31, *Sci. Rep.* 11 (2021) 2774.
- [22] L.M. Calado, M.G. Taryba, Y. Morozov, M.J. Carmezim, M.F. Montemor, Novel smart and self-healing cerium phosphate-based corrosion inhibitor for AZ31 magnesium alloy, *Corros. Sci.* 170 (2020).
- [23] M.S. Reisch, Confronting the looming hexavalent chromium ban, *Chem. Eng. N.* 95 (2017) 28–29.
- [24] E.V.S. Hessel, Y.C.M. Staal, A.H. Piersma, S.P. den Braver-Sewradj, J. Ezendam, Occupational exposure to hexavalent chromium. Part I. Hazard assessment of non-cancer health effects, *Regul. Toxicol. Pharmacol.* 126 (2021) 105048.
- [25] A. Kokalj, M. Lozinsek, B. Kapun, P. Taheri, S. Neupane, P. Losada-Pérez, C. Xie, S. Stavber, D. Crespo, F.U. Renner, A. Mol, I. Milošev, Simplistic correlations between molecular electronic properties and inhibition efficiencies: do they really exist? *Corros. Sci.* (2021) 179.
- [26] A. Kokalj, C. Xie, I. Milošev, D. Crespo, How relevant are molecular electronic parameters for predicting corrosion inhibition efficiency: imidazoles as corrosion inhibitors of Cu/Zr materials in NaCl solution, *Corros. Sci.* (2021) 193.
- [27] Y. Song, D. Shan, E.-H. Han, Pitting corrosion of a Rare Earth Mg alloy GW93, *J. Mater. Sci. Technol.* 33 (2017) 954–960.
- [28] H. Wang, Y. Song, D. Shan, E.-H. Han, Effects of corrosive media on the localized corrosion forms of Mg-Zn alloy, *Corros. Commun.* 2 (2021) 24–32.
- [29] E.L. Boland, R.N. Shirazi, J.A. Grogan, P.E. McHugh, Mechanical and corrosion testing of magnesium WE43 specimens for pitting corrosion model calibration, *Adv. Eng. Mater.* 20 (2018).
- [30] D. Mei, Y. Li, Y. Tian, Q. Zhang, M. Liu, S. Zhu, L. Wang, S. Guan, The effect of selected corrosion inhibitors on localized corrosion of magnesium alloy: The expanded understanding of "inhibition efficiency", *Corros. Sci.* (2024) 226.
- [31] A.H. Lipkus, Q. Yuan, K.A. Lucas, S.A. Funk, W.F. Bartelt, R.J. III, A.J. Schenck, Tripe, structural diversity of organic chemistry. a scaffold analysis of the CAS registry, *J. Org. Chem.* 73 (2008) 4443–4451.
- [32] D.A. Erlanson, S.W. Fesik, R.E. Hubbard, W. Jahnke, H. Jhoti, Twenty years on: the impact of fragments on drug discovery, *Nat. Rev. Drug Discov.* 15 (2016) 605–619.
- [33] T. Würger, D. Mei, B. Vaghefinazari, D.A. Winkler, S.V. Lamaka, M. L. Zheludkevich, R.H. Meißner, C. Feiler, Exploring structure-property relationships in magnesium dissolution modulators, *npj Mater. Degrad.* 5 (2021).
- [34] D.A. Winkler, M. Breedon, P. White, A.E. Hughes, E.D. Sapper, I. Cole, Using high throughput experimental data and in silico models to discover alternatives to toxic chromate corrosion inhibitors, *Corros. Sci.* 106 (2016) 229–235.
- [35] D.A. Winkler, F.R. Burden, Robust QSAR models from novel descriptors and bayesian regularised neural networks, *Mol. Simul.* 24 (2000) 243–258.
- [36] T. Le, V.C. Epä, F.R. Burden, D.A. Winkler, Quantitative structure–property relationship modeling of diverse materials properties, *Chem. Rev.* 112 (2012) 2889–2919.
- [37] D. Costa, T. Ribeiro, P. Cornette, P. Marcus, DFT modeling of corrosion inhibition by organic molecules: carboxylates as inhibitors of aluminum corrosion, *J. Phys. Chem. C* 120 (2016) 28607–28616.
- [38] B.D. Chambers, S.R. Taylor, M.W. Kendig, Rapid discovery of corrosion inhibitors and synergistic combinations using high-throughput screening methods, *Corrosion* 61 (2005) 480–489.
- [39] T.H. Muster, A.E. Hughes, S.A. Furman, T. Harvey, N. Sherman, S. Hardin, P. Corrigan, D. Lau, F.H. Scholes, P.A. White, M. Glenn, J. Mardel, S.J. Garcia, J.M. C. Mol, A rapid screening multi-electrode method for the evaluation of corrosion inhibitors, *Electrochim. Acta* 54 (2009) 3402–3411.
- [40] S. Kallip, A.C. Bastos, M.L. Zheludkevich, M.G.S. Ferreira, A multi-electrode cell for high-throughput SVET screening of corrosion inhibitors, *Corros. Sci.* 52 (2010) 3146–3149.
- [41] P.A. White, G.B. Smith, T.G. Harvey, P.A. Corrigan, M.A. Glenn, D. Lau, S. G. Hardin, J. Mardel, T.A. Markley, T.H. Muster, N. Sherman, S.J. Garcia, J.M. C. Mol, A.E. Hughes, A new high-throughput method for corrosion testing, *Corros. Sci.* 58 (2012) 327–331.
- [42] A.V. Zabula, S. Dey, J.R. Robinson, T. Cheisson, R.F. Higgins, G. Bhargava, R. C. Nahas, D. Cinoman, M. Kerins, E.C. Houze, E.J. Schelter, Screening of molecular lanthanide corrosion inhibitors by a high-throughput method, *Corros. Sci.* 165 (2020).
- [43] P.A. White, G.E. Collis, M. Skidmore, M. Breedon, W.D. Ganther, K. Venkatesan, Towards materials discovery: assays for screening and study of chemical interactions of novel corrosion inhibitors in solution and coatings, *N. J. Chem.* 44 (2020) 7647–7658.
- [44] Y. Qiu, X. Tu, X. Lu, J. Yang, A novel insight into synergistic corrosion inhibition of fluoride and DL-malate as a green hybrid inhibitor for magnesium alloy, *Corros. Sci.* 199 (2022).
- [45] M. Liu, Q. Zhang, X. Tang, C. Liu, D. Mei, L. Wang, S. Zhu, M.L. Zheludkevich, S. Lamaka, S. Guan, Effect of medium renewal mode on the degradation behavior of Mg alloys for biomedical applications during the long-term in vitro test, *Corros. Sci.* (2024).
- [46] B.G. Koushik, N. Van den Steen, M.H. Mamme, Y. Van Ingelgem, H. Terryn, Review on modelling of corrosion under droplet electrolyte for predicting atmospheric corrosion rate, *J. Mater. Sci. Technol.* 62 (2021) 254–267.
- [47] M. Nienaber, K.U. Kainer, D. Letzig, J. Bohlen, Processing effects on the formability of extruded flat products of magnesium alloys, *Front. Mater.* 6 (2019).
- [48] U.C. Nwaogu, C. Blawert, N. Scharnagl, W. Dietzel, K.U. Kainer, Influence of inorganic acid pickling on the corrosion resistance of magnesium alloy AZ31 sheet, *Corros. Sci.* 51 (2009) 2544–2556.
- [49] U.C. Nwaogu, C. Blawert, N. Scharnagl, W. Dietzel, K.U. Kainer, Effects of organic acid pickling on the corrosion resistance of magnesium alloy AZ31 sheet, *Corros. Sci.* 52 (2010) 2143–2154.
- [50] 2013, Standard Guide for Examination and Evaluation of Pitting Corrosion..
- [51] G. Williams, A.J. Coleman, H.N. McMurray, Inhibition of aluminium Alloy AA2024-T3 pitting corrosion by copper complexing compounds, *Electrochim. Acta* 55 (2010) 5947–5958.
- [52] J. Chen, J. He, L. Li, Spectroscopic insight into the role of SDBS on the interface evolution of Mg in NaCl corrosive medium, *Corros. Sci.* 182 (2021).
- [53] Y. Li, J. Ma, G. Wang, F. Ren, Y. Zhu, Y. Song, Investigation of sodium phosphate and sodium dodecylbenzenesulfonate as electrolyte additives for AZ91 magnesium-air battery, *J. Electrochem. Soc.* 165 (2018) A1713–A1717.
- [54] H. Gao, Q. Li, Y. Dai, F. Luo, H.X. Zhang, High efficiency corrosion inhibitor 8-hydroxyquinoline and its synergistic effect with sodium dodecylbenzenesulphonate on AZ91D magnesium alloy, *Corros. Sci.* 52 (2010) 1603–1609.
- [55] X. Guo, M. An, P. Yang, H. Li, C. Su, Effects of benzotriazole on anodized film formed on AZ31B magnesium alloy in environmental-friendly electrolyte, *J. Alloy. Compd.* 482 (2009) 487–497.
- [56] J.-L. Wang, C. Ke, K. Pohl, N. Birbilis, X.-B. Chen, The unexpected role of benzotriazole in mitigating magnesium alloy corrosion: a nucleating agent for crystalline nanostructured magnesium hydroxide film, *J. Electrochem. Soc.* 162 (2015) C403.
- [57] I.A. Kartsonakis, S.G. Stanciu, A.A. Matei, E.K. Karaxi, R. Hristu, A. Karantonis, C. A. Charitidis, Evaluation of the protective ability of typical corrosion inhibitors for magnesium alloys towards the Mg ZK30 variant, *Corros. Sci.* 100 (2015) 194–208.
- [58] N. Dinodi, A.N. Shetty, Alkyl carboxylates as efficient and green inhibitors of magnesium alloy ZE41 corrosion in aqueous salt solution, *Corros. Sci.* 85 (2014) 411–427.
- [59] L.I. Fockaert, T. Würger, R. Unbehau, B. Boelen, R.H. Meißner, S.V. Lamaka, M. L. Zheludkevich, H. Terryn, J.M.C. Mol, ATR-FTIR in Kretschmann configuration integrated with electrochemical cell as in situ interfacial sensitive tool to study corrosion inhibitors for magnesium substrates, *Electrochim. Acta* 345 (2020).
- [60] I. Milošev, D. Zimerl, C. Carrière, S. Zanna, A. Seyeux, J. Iskra, S. Stavber, F. Chiter, M. Poberžnik, D. Costa, A. Kokalj, P. Marcus, Editors' choice—the effect of anchor group and alkyl backbone chain on performance of organic compounds as corrosion inhibitors for aluminum investigated using an integrative experimental-modeling approach, *J. Electrochem. Soc.* 167 (2020).
- [61] B. Vaghefinazari, S.V. Lamaka, E. Gazeinbiller, K. Yasakau, C. Blawert, M. Serdechnova, N. Scharnagl, D.C.F. Wieland, M.L. Zheludkevich, Corrosion inhibition of decylphosphonate on bare and PEO-coated Mg alloy, *Corros. Sci.* 226 (2024).
- [62] T. Hauffman, O. Blajiev, J. Snaauwerta, C. van Haesendonck, A. Hubin, H. Terryn, Study of the self-assembling of n-octylphosphonic acid layers on aluminum oxide, *Langmuir* 24 (2008) 13450–13456.
- [63] D. Mercier, J. Świątowska, E. Protopopoff, S. Zanna, A. Seyeux, P. Marcus, Inhibition of Mg corrosion by sulfur blocking of the hydrogen evolution reaction on iron impurities, *J. Electrochem. Soc.* 167 (2020).
- [64] C. Song, C. Wang, D. Mercier, B. Vaghefinazari, A. Seyeux, D. Snihirova, D.C. F. Wieland, P. Marcus, M.L. Zheludkevich, S.V. Lamaka, Corrosion inhibition mechanism of 2,6-pyridinedicarboxylate depending on magnesium surface treatment, *Corros. Sci.* 229 (2024).
- [65] A.D. John, Lange's handbook of chemistry. in: Universitas Of Tennessee Knoxville, Fifteenth Edition, Mc. Graw Hill Inc, Conference, New York, 1999.
- [66] T.G. Harvey, S.G. Hardin, A.E. Hughes, T.H. Muster, P.A. White, T.A. Markley, P. A. Corrigan, J. Mardel, S.J. Garcia, J.M.C. Mol, A.M. Glenn, The effect of inhibitor structure on the corrosion of AA2024 and AA7075, *Corros. Sci.* 53 (2011) 2184–2190.
- [67] ASTM G1-03: Standard Practice for Preparing, Cleaning, and Evaluating Corrosion Test Specimens, in, ASTM, 2004.